RSC Advances

PAPER

View Article Online
View Journal | View Issue

Cite this: *RSC Adv.*, 2026, **16**, 8136

Chitosan-functionalized Ag–Cu-ferrite nanocomposite as a high-performance electrochemical sensor for ascorbic acid detection: experimental and theoretical exploration

Hana Boucheta,[ab] Emna Zouaoui,[bc] Mina Boulkroune,[de] Hana Ferkous,*[fg] Belgacem Bezzina,[h] Mohammed Rabeh Makhlouf,[i] Hichem Tahraoui,[jk] Hanan Alhussain,[l] Ahmed Fawzy,[m] Magdi E. A. Zaki,[l] Ahmed A. Farag[n] and Arafat Toghan*[l]

The present research introduces an electrochemical detection system constructed from chitosan-functionalized Ag–Cu-ferrite nanoparticles ($Ag_{0.02}Cu_{0.98}Fe_2O_4$@chitosan). This nanocomposite-based sensor provides an efficient approach for the targeted measurement of ascorbic acid (AA). Characterization using XRD and FTIR techniques confirmed the effective incorporation of chitosan into the $Ag_{0.02}Cu_{0.98}Fe_2O_4$ spinel framework. Using CV (cyclic voltammetry), the $Ag_{0.02}Cu_{0.98}Fe_2O_4$@chitosan-supported CPE electrode exhibited an oxidation peak at +0.28 V compared to +0.55 V for bare CPE in phosphate buffer (pH = 7), highlighting its superior electrocatalytic achievement. The current response exhibited a linear dependence with the square root of the scan rate (R^2 = 0.9895), suggesting that the process is governed by diffusion. Sensitivities of 411.59 μA mM^{-1} cm^2 and 327.31 μA mM^{-1} cm^2 were achieved by the sensor over two distinct linear ranges, 100–300 μM and 300 μM–13 mM. With a high degree of certainty, the limit of detection (LOD) was recorded at 89 μM. The fabricated electrode displayed high selectivity within the presence of commonly used interferents (glucose, fructose, sucrose, NaCl, and KCl), as well as impressive reproducibility (RSD = 1.96%) and repeatability (RSD = 1.15%).It also achieved a superior AA recovery rate of up to 98% in a real sample, demonstrating its consistency and reliability. DFT computations confirmed AA's chemical reactivity through a moderate energy gap (ΔE = 5.42 eV) and identified reactive sites on oxygen atoms using molecular electrostatic potential (MESP) and Fukui function analysis (FIs). Additionally, Monte Carlo simulations (MCS) revealed a highly favorable adsorption energy of −26.65 kcal mol^{-1} for AA on the $Ag_{0.02}Cu_{0.98}Fe_2O_4$@chitosan-CPE surface, validating the strong affinity of the target analyte toward the modified electrode. Overall, the integration of chitosan into the $Ag_{0.02}Cu_{0.98}Fe_2O_4$ nanostructure significantly improved the electrocatalytic efficiency, selectivity, and stability of the sensor, making it an excellent option for practical applications in vitamin C detection.

Received 5th December 2025
Accepted 30th January 2026

DOI: 10.1039/d5ra09413e

rsc.li/rsc-advances

[a]*Laboratory of Physico-Chemistry Research on Surfaces and Interfaces (LRPCSI), University of 20 August 1955, Skikda 21000, Algeria*

[b]*Laboratory of Catalysis, Bio-process and Environment, Faculty of Technology, University of 20 August 1955, Skikda 21000, Algeria*

[c]*LACReSNE Laboratoire d'application de la Chimie aux Ressources et Substances Naturelles en Environnement, Faculté des Sciences de Bizerte, Université de Carthage, 7021 Jarzouna Bizerte, Tunisia*

[d]*Environmental and Structural Molecular Chemistry Research Unit (UR-CHEMS), Faculty of Exact Sciences, University Constantine 1, Constantine 25000, Algeria*

[e]*Department of Chemistry, Faculty of Exact Sciences, University of Constantine 1, Constantine 25000, Algeria*

[f]*Laboratory of Mechanical Engineering and Materials, Faculty of Technology, University of 20 August Skikda, Skikda 21000, Algeria. E-mail: h.ferkous@univ-skikda.dz*

[g]*Département de Technologie, Université de Skikda, Skikda 21000, Algeria*

[h]*Research Center in Industrial Technologies (CRTI), P.O.BOX 64, Chéraga, Algiers, 16014, Algeria*

[i]*Laboratoire d'Analyses Industrielles et Génie Des Matériaux, Université 8 Mai 1945 Guelma 24000, Guelma, BP 401, Algeria*

[j]*Département Science de la matière, Faculté des Sciences, UniversitéYahia Fares, Médéa, Algeria*

[k]*Laboratory of Reaction Engineering, Department of Mechanical and Process Engineering, University of Science and Technology HouariBoumediene (USTHB), Algiers-Bab Ezzouar 16111, Algeria*

[l]*Chemistry Department, College of Science, Imam Mohammad Ibn Saud Islamic University (IMSIU), Riyadh 11623, Saudi Arabia. E-mail: aatahmed@imamu.edu.sa*

[m]*Chemistry Department, Faculty of Science, Assiut University, Assiut 71516, Egypt*

[n]*Egyptian Petroleum Research Institute (EPRI), Nasr City, Cairo 11727, Egypt*

1 Introduction

Vitamin C (ascorbic acid, AA) is a powerful water-soluble antioxidant that neutralizes harmful free radicals (reactive oxygen molecules) that can damage cells and DNA. It is primarily obtained from fruits and vegetables and is widely present in many dietary sources.[1–4] As a vital nutrient, vitamin C contributes to the prevention and treatment of several disorders, including skin conditions, infertility, cancer, and liver diseases.[5–7] Unlike most mammals, the human body is unable to synthesize Ascorbic acid endogenously, making its dietary intake indispensable to avoid deficiency-related complications.[8–10] The recommended daily amount of vitamin C ranges from 75 to 90 mg for adults according to the institution of Medicine's Recommended Dietary Allowances (RDA).[11,12] Given its wide biological significance and importance in food and health monitoring, the accurate quantification of AA is crucial for ensuring product quality, safety, and therapeutic efficiency.[13,14] Different approaches have been utilized to find out AA levels, including chromatographic, spectroscopic, and electrochemical techniques.[15,16] Owing to their remarkable accuracy, low cost, versatility, sensitivity and rapid response, electrochemical processes have attracted considerable interest, leading to the engineering of numerous sensors and electrochemical platforms for detecting AA in complex matrices[16–19]

Carbon paste electrodes (CPEs) offer an economical and adaptable platform for electrochemical sensing owing to their simple preparation and renewable surface.[20–22] To enhance sensor performance, their surfaces are often modified with conducting polymers or nanoparticles (NPs), which improve conductivity, selectivity, and sensitivity.[23–25] Recently, considerable interest has been devoted to spinel ferrite (Fe_2O_4)-based materials with the general formula $M^{2+}Fe_2O_4$ for electrochemical applications, owing to their structural stability, redox activity, and tunable electrical properties.[26] The nature of the divalent metal ion (M^{+2}) plays a crucial role in governing charge transport, magnetic behavior, and electrocatalytic performance. Accordingly, previous investigations have shown that adding Co and Zn to $CuFe_2O_4$ leads to an increase in crystal size and lattice parameters.[27] Indeed, among ferrite-based materials, Cu-ferrite ($CuFe_2O_4$) has attracted increasing attention due to its chemical stability, redox versatility, and functional adaptability, making it suitable for sensing applications.[28] On the other hand, many conductive polymers, such as chitosan, polyaniline, and polypyrrole, are frequently used to modify sensor surfaces by improving the material's conductivity and surface area, thus providing a selective and efficient interaction for target detection.[29,30] Chitosan, in particular, is a natural polysaccharide derived from chitin, commonly found in shrimp shells, crabs, and fungi. It exhibits several attractive features such as non-toxicity, biodegradability, antimicrobial activity, and excellent film-forming ability. Furthermore, incorporating NPs into the chitosan matrix (NPs-based chitosan) enhances sensor performance.[31,32] The hybrid material leverages the best properties of both components, creating a more robust and efficient sensing platform than either could provide on its own.

However, some Cu-ferrite/based chitosan sensors have been previously reported for detecting AA and others,[31,32] in which chitosan acts as a binding agent and helps stabilize $CuFe_2O_4$ NPs, ensuring good adhesion of the film to the electrode surface. In these systems, although their electrochemical characteristics are improved by increasing the surface area and/or adsorption properties, performance and sensitivity still need improvement. Therefore, the introduction of a small amount of monovalent ions (*e.g.* Ag^+) with a different ionic radius to partially substitute the divalent ions (Cu^{2+}) in the $CuFe_2O_4$ lattice (forming an Ag-dopped $CuFe_2O_4$-chitosan), may create crystal defects that greatly enhance its ionic conductivity, and as a result the surface reactivity, electrocatalytic, and sensing capability are expected to improve. This compositional tuning, combined with chitosan acting as an active interfacial modifier rather than a passive binder, is expected to fundamentally distinguish the present sensor from previously reported $CuFe_2O_4$-chitosan based systems.

To address the above-mentioned challenges, in this work a Ag-doped $CuFe_2O_4$-chitosan nanocomposite modified-CPE ($Ag_{0.02}$-$Cu_{0.98}Fe_2O_4$@chitosan-CPE) was fabricated, and first applied to precisely detect AA. For comparison, electrode-free chitosan was also prepared and named $Ag_{0.02}Cu_{0.98}Fe_2O_4$-CPE, alongside the bare CPE electrode. The phase structure and interfacial properties of the mixed-valence engineered materials were investigated using X-ray diffraction (XRD), and Fourier-transform infrared spectroscopy (FTIR). In addition, scanning electron microscopy (SEM) and energy-dispersive X-ray spectroscopy (EDX) were performed to examine the surface morphology and elemental composition of developed samples. Cyclic voltammetry (CV) was used to analyze their electrochemical performance towards AA. This was achieved experimentally by evaluating several key metrics such sensitivity, linear response range, limit of detection (LOD), selectivity, repeatability, and reproducibility. Furthermore, computational methods (DFT and Monte Carlo simulations) were used to model the behavior of AA and its interactions with the modified electrode surfaces, providing a complementary theoretical insight into the experimental observations.

2 Experimental

2.1 Materials

From BIOCHEM, $Fe(NO_3)_3 \cdot 9H_2O$ and $Cu(NO_3)_2 \cdot 3H_2O$ were purchased. $AgNO_3$, NaOH and CH_3COOH were obtained from AGENOR (Algeria), PROLABO and FLUKA, respectively. Commercial chitosan and carbon were used as received. Distilled water and paraffin oil (purchased from ISOPHARM ALGERIA) were used throughout the experiments, while fructose and sucrose were obtained from Sigma-Aldrich. Ascorbic acid (AA), KCl, NaCl and D-glucose were obtained from LABOSI, PROLAB, BIOCHEM, and TM MEDIA respectively. A 0.1 M PBS (phosphate buffer) solution at pH 7.0 was prepared from NaH_2PO_4 and Na_2HPO_4 sourced from BIOCHEM.

2.2 Functionalization of $Ag_{0.02}Cu_{0.98}Fe_2O_4$

A simple co-precipitation method was employed to synthesize the $Ag_{0.02}Cu_{0.98}Fe_2O_4$ catalyst prior to further processing. In this procedure, the appropriate amounts of copper nitrate, $Fe(NO_3)_3$, and $AgNO_3$ were dissolved in distilled water. The mixture was

magnetically stirred for the required time, after which NaOH solution gradually added drop by drop until reaching pH 11. The resulting precipitate was then filtered, rinsed thoroughly with distilled water, and left to dry overnight at 80 °C, then sintered at 750 °C for 4 h. The $Ag_{0.02}Cu_{0.98}Fe_2O_4$ functionalized chitosan composite was prepared following the procedure of Boultif W. *et al.*[21] Initially, a measured amount of chitosan was solubilized in 5% (v/v) acetic acid with continuous agitation for 24 h. The synthesized $Ag_{0\cdot02}Cu_{0\cdot98}Fe_2O_4$ NPs were then mixed with the chitosan mixture while continuously stirring. To induce composite formation, designated as $Ag_{0\cdot02}Cu_{0\cdot98}Fe_2O_4$@chitosan, a 0.5 M NaOH solution was gradually introduced until precipitation occurred. Finally, the precipitate was washed well with water and left to dry at 100 °C, and the material was thus ready.

2.3 Sensors fabrication

To design the working electrodes (WE's), carbon powder and paraffin oil were combined manually in an agate mortar for 30 min until a uniform paste was achieved (Scheme 1). To guarantee electrical contact, the resultant paste was first placed into the barrel of a syringe that had been equipped with a copper wire. It was then allowed to dry naturally. $Ag_{0\cdot02}Cu_{0\cdot98}Fe_2O_4$ or $Ag_{00}Cu_{0\cdot98}Fe_2O_4$@chitosan was added to the carbon-oil mixture at a ratio of 20 : 65 : 15 (w/w) to create enhanced electrodes employing the same process. Paper was used to smooth the electrode surface, and distilled water was used to clean it before application.[33] The labels for the changed electrode were $Ag_{0\cdot02}Cu_{0\cdot98}Fe_2O_4$-CPE, $Ag_{0\cdot02}Cu_{0\cdot98}Fe_2O_4$@chitosan-CPE, and CPE, accordingly.

2.4 Characterization techniques

XRD analysis was performed using Cu Kα radiation ($\lambda = 1.54056$ Å) on a Bruker D8 Advance diffractometer to verify the phase and crystal structure of the designed nanostructured. FTIR spectra (Bruker Vertex 70 spectrometer) were recorder in the region of 4000–500 cm^{-1} to identify functional groups and evaluate inter- and intramolecular interactions. The surface morphology and elemental composition were examined by scanning electron microscopy (SEM) coupled with energy-dispersive X-ray spectroscopy (EDX), using a Thermo Scientific Prisma E instrument.

2.5 Electrochemical measurements

To conduct all electrochemical tests, a GAMRY Potentiostat/Galvanostat/ZRA (Reference 3000) was utilized at ambient temperature. Reference and auxiliary electrodes were copper wire and Ag/AgCl, respectively. Additionally, $Ag_{0.02}Cu_{0.98}Fe_2O_4$-CPE, $Ag_{0.02}Cu_{0.98}Fe_2O_4$@chitosan-CPE, and CPE were used as WE's. The ability of electrochemical identification was assessed in 0.1 M of PBS (pH 7.0) both in the presence and absence of AA (5 mM). CVs were performed in a potential window ranging from −0.4 V to +0.8 V at a scan rate of 50 mV s^{-1}.

To evaluate the LOD, linearity, and selectivity, serial additions of different AA levels were made. In the event of common interfering substances such glucose, fructose, sucrose, KCl, and NaCl, the modified electrodes' selectivity was further evaluated. Three separately manufactured electrodes under identical circumstances were used to test reproducibility, and the same modified electrode was used to do 15 consecutive tests to test repeatability.

2.6 Computational studies

2.6.1 DFT calculations. Computations were employed to model the electronic structure, the chemical reactivity and intramolecular charge transfer characteristics of AA, with the specific B3LYP functional and the DNP (double numerical plus

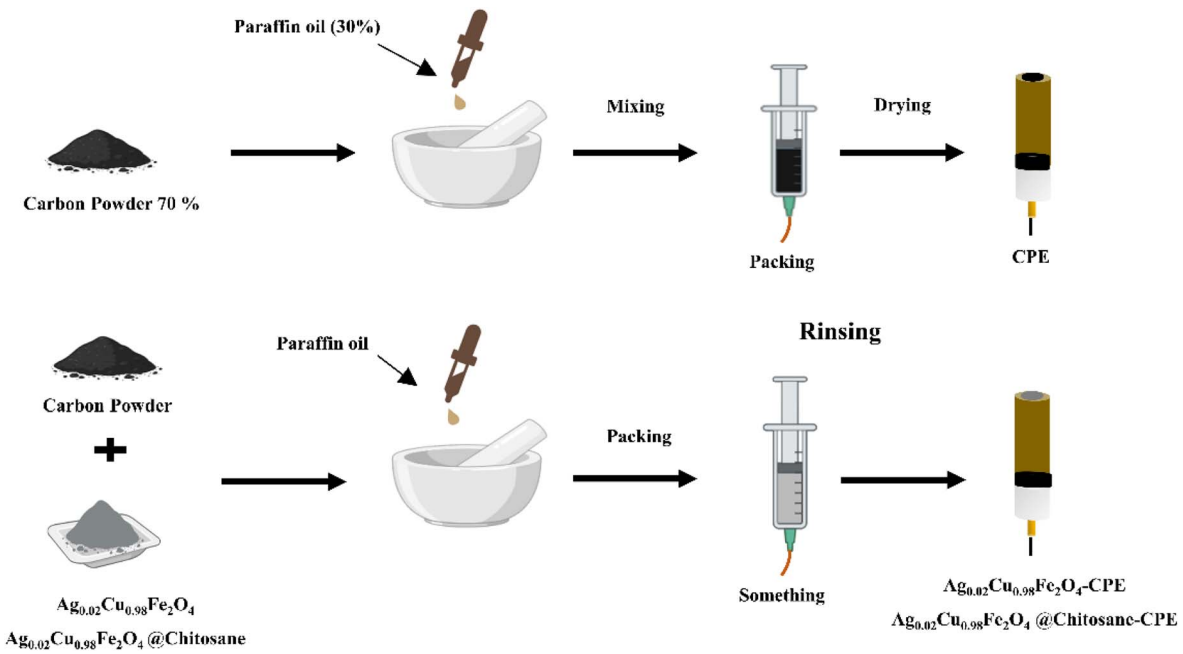

Scheme 1 Schematic diagram of the sensor fabrication steps.

polarization) basis set. DMol^3 software is used to perform all calculations.[34,35]

Subsequently, frontier molecular orbital (FMO) analysis was conducted to identify the HOMO and LUMO energy levels. Key descriptors used to evaluate molecular stability and reactivity include the energy band gap (ΔE_{gap}), HOMO and LUMO energies, global hardness (η), electronegativity (χ), and global softness (σ). Reactivity descriptors equations are as follows:

$$I = -E_{HOMO} \quad (1)$$

$$A = -E_{LUMO} \quad (2)$$

$$\Delta E_{gap} = I - A \quad (3)$$

$$\chi = \frac{1}{2}(I - A) \quad (4)$$

$$\eta = \frac{1}{2}(I - A) \quad (5)$$

$$\sigma = \frac{1}{\eta} \quad (6)$$

These descriptors provide insight into the electronic behavior and potential reaction mechanisms of the molecule.[36–38]

Furthermore, the most reactive atomic sites of AA were predicted using FIs (f_k^-, $f_k^+$and f_k^0).[39,40]

$$f_k^-(\text{for electrophilic attack}) = q_k(N) - q_k(N-1) \quad (7)$$

$$f_k^+(\text{for nucleophilic attack}) = q_k(N+1) - q_k(N) \quad (8)$$

$$f_k^0(\text{for radical attack}) = \frac{1}{2}[q_k(N+1) - q_k(N-1)] \quad (9)$$

The electronic populations of atom k is represented by $q_k(N)$ for neutral, $q_k(N+1)$ for anionic, and $q_k(N-1)$ for cationic species.[41,42]

2.6.2 Monte Carlo simulation (MCS). The electrocatalytic activity of CPE with $Ag_{0.02}Cu_{0.98}Fe_2O_4$ and $Ag_{0.02}Cu_{0.98}Fe_2O_4$@chitosan was systematically examined using MCS calculations. Additionally, the nature of electrostatic interactions between AA compounds and both unmodified and modified CPE surfaces was examined. By closely replicating experimental conditions, these simulations provided detailed insights into how surface modifications alter the electrode's adsorption properties and charge distribution, thereby influencing the efficiency of AA oxidation. This computational approach not only elucidates the mechanistic role of each modification in enhancing sensor performance, but also guides the rational design of more effective electrochemical sensors for AA detection.

The $Ag_{0.02}Cu_{0.98}Fe_2O_4$ and $Ag_{0.02}Cu_{0.98}Fe_2O_4$@chitosan nanoclusters, alongside the carbon sheet surfaces of the CPE, were constructed using the build tool in Materials Studio 2017.[43] The CPE was represented by a two-dimensional graphite model comprising two carbon layers aligned along the (001) crystallographic plane. MCS simulations were performed with the Adsorption Locator module employing a Universal Force Field[44,45] to accurately predict the adsorption energies and preferred configurations of AA molecules on each electrode surface. This modeling approach enabled a detailed comparative analysis of AA interaction dynamics across pristine and modified electrode interfaces, providing crucial insight into the molecular-level mechanisms governing sensor performance.

The adsorption energy (E_{ads}) depends on the equation of the adsorbent/substrate interactions:[46,47]

$$E_{ads} = E_{Tot} - (E_{Substrate} + E_{Adsorbate}) \quad (10)$$

where: E_{Tot} = total energy, $E_{Substrate}$ = energy of substrate and $E_{Adsorbate}$ = energy of adsorbate.

3 Results and discussion

3.1 Chemistry

3.1.1 XRD measurements. The phase structure of commercial chitosan, $Ag_{0.02}Cu_{0.98}Fe_2O_4$, and $Ag_{0.02}Cu_{0.98}Fe_2O_4$@chitosan was determined by XRD (Fig. 1). Chitosan exhibited a typical broad diffraction peak at ≈20.17°, confirming its semi-crystalline nature.[48] The diffraction pattern of the Ag-doped sample ($Ag_{0.02}Cu_{0.98}Fe_2O_4$) confirmed the formation of a tetragonal Cu-ferrite phase (JCPDS card no. 01-072-1174). The main diffraction peaks were observed at the 2θ values: 18.34°, 29.87°, 34.50°, 36.04°, 37.17°, 41.43°, 44.04°, 54.13°, 57.22°, 58.17°, 62.06°, 64.05°, and 74.83°. These peaks correspond to the (101), (112), (103), (211), (202), (004), (213), (312), (303), (321), (224), (400), and (413) planes of the spinel ferrite structure, respectively. Weak reflections are also detected at 2θ = 38.13°, 43.82°, 64.45°, and 77.40°, which are attributed to the (111), (200), (220), and (311) planes of AgO (JCPDS card no. 03-065-8428), indicating a low content of Ag species in the manufactured system. For the $Ag_{0.02}Cu_{0.98}Fe_2O_4$@chitosan composite, the characteristic reflections of the spinel ferrite

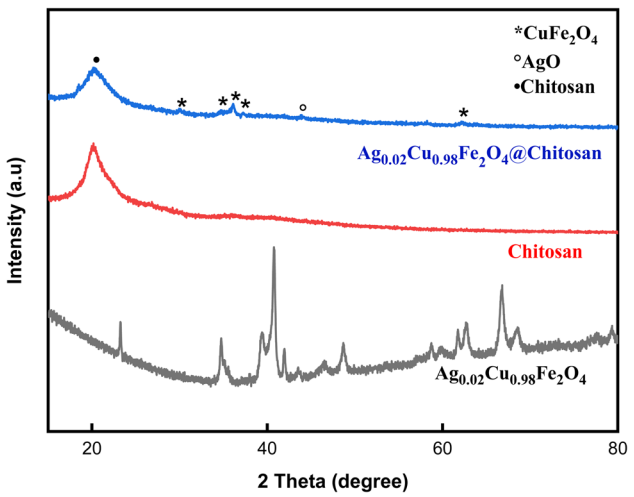

Fig. 1 XRD patterns of pure chitosan, $Ag_{0.02}Cu_{0.98}Fe_2O_4$, and $Ag_{0.02}Cu_{0.98}Fe_2O_4$@chitosan composite.

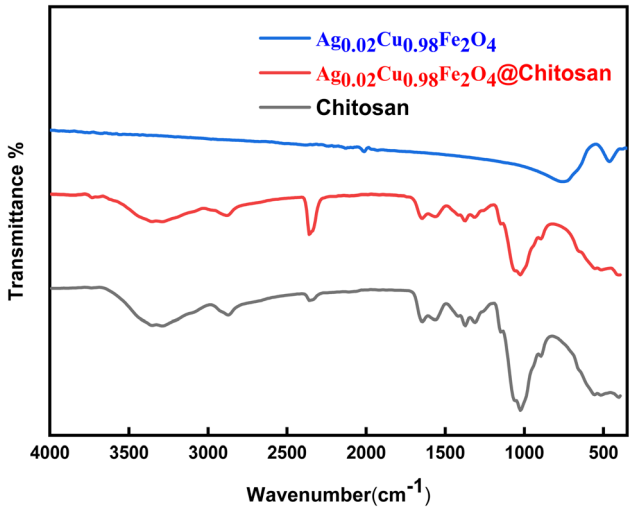

Fig. 2 Comparison of FTIR spectra of pure chitosan, $Ag_{0.02}Cu_{0.98}Fe_2O_4$, and $Ag_{0.02}Cu_{0.98}Fe_2O_4$@chitosan composite.

phase are preserved, indicating that chitosan functionalization does not alter the crystal structure of the ferrite. However, slight peak shifts and additional peak broadening are observed, which can be ascribed to interfacial stress and surface interactions between the ferrite NPs and the chitosan matrix. The coexistence of a broad peak at ≈20.3° and the peaks of Ag–Cu-ferrite NPs provides clear evidence for a successful fabrication of chitosan-functionalized Ag–Cu-Ferrite nanocomposite.

By applying the Debye–Scherer equation to several well-defined diffraction peaks of the ferrite phase, the average crystal of the Ag-doped sample ($Ag_{0.02}Cu_{0.98}Fe_2O_4$) was estimated to be size 18.7 nm.[49,50] To further evaluate lattice distortion, the microstrain was calculated using the Williamson–Hall method, resulting in a strain value of 1.20×10^{-3}. The crystal size calculated using the Williamson–Hall method was 21.2 nanometers, consistent with Shearer's estimate, thus confirming the reliability of the analysis. Interestingly, the observable peak broadening in XRD and lattice stress can be attributed to the ionic radius mismatch between Ag^+ and Cu^{2+}, leading to local lattice distortion and the resulting improvement in ionic transport properties.

3.1.2 FT-IR. The FTIR spectra provide valuable insights into the chemical structure and confirm the functionalization of $Ag_{0.02}Cu_{0.98}Fe_2O_4$ with chitosan through the presence of characteristic vibrational bands. Recorded in the 4000–400 cm^{-1} range (Fig. 2), the spectra of both chitosan and $Ag_{0.02}Cu_{0.98}Fe_2O_4$@chitosan show a broad absorption band at 3288 cm^{-1}, corresponding to N–H stretching vibrations,[22] along with a band at 2872 cm^{-1} attributed to C–H stretching.[51–54] Peaks at 1645, 1563, and 1312 cm^{-1} are assigned to C=O stretching of amide I, N–H bending of primary amines, and C–H bending, respectively.[20,21,55] The band near 1024 cm^{-1} indicates C–O stretching,[56] while absorption bands in the 500–800 cm^{-1} region are linked to Ag–O, Cu–O, and Fe–O stretching vibrations, confirming the integration of the metal oxide phase into the composite.

Comparative analysis of the spectra for chitosan and $Ag_{0.02}Cu_{0.98}Fe_2O_4$@chitosan reveals a decrease in peak intensities in the latter, indicating strong interactions between the chitosan matrix and the $Ag_{0.02}Cu_{0.98}Fe_2O_4$ NPs.[22,26] In addition to the intensity variations, the persistence and modification of the chitosan characteristic bands after functionalization indicate a change in the local chemical environment of the $-NH_2$ and –OH groups. Such behavior is consistent with coordination and hydrogen-bonding interactions between these functional groups and surface metal ions ($Fe^{3+}/Cu^{2+}/Ag^+$) of the Ag-doped sample ($Ag_{0.02}Cu_{0.98}Fe_2O_4$). In the case of a simple physical mixture, a superposition of the individual FTIR spectra without noticeable intensity changes or band perturbation would be expected. Therefore, the observed spectral features provide evidence of chemical interaction at the chitosan-ferrite interface rather than mere physical mixing.

3.1.3 SEM-EDX. The surface morphology and elemental composition of the fabricated materials were identified by SEM and EDX. Fig. 3 shows SEM images of $Ag_{0.02}Cu_{0.98}Fe_2O_4$ (Fig. 3b) compared to pure $CuFe_2O_4$ NPs (Fig. 3a), demonstrating the successful incorporation of Ag species on the surface of $CuFe_2O_4$. The SEM micrograph of native $CuFe_2O_4$ NPs shows an irregular clustering of varying diameters, a result of their inherent magnetic characteristics.[57,58] Whereas, the SEM image of the silver-doped sample ($Ag_{0.02}Cu_{0.98}Fe_2O_4$) clearly showed the clustering of spherical Ag species.[59] The corresponding EDX analysis for $CuFe_2O_4$ and $Ag_{0.02}Cu_{0.98}Fe_2O_4$ is displayed in Fig. 3c and d. The EDX spectrum confirmed the presence of Ag alongside Fe, Cu, and O, consistent with the intended composition. The detected Ag content corresponds to a low doping level, which is expected given the nominal $Ag_{0.02}$-composition and the semi-quantitative nature of EDX for trace elements. Interestingly, no Ag-rich secondary phases were detected, and the homogeneous elemental distribution supports successful incorporation rather than surface segregation. These findings align with previous studies indicating the presence of a single-phase spinel structure.[60]

3.2 Sensing of AA

The electrochemical detection of AA in PBS (pH 7.0) using both modified and unmodified CPE is illustrated in Fig. 4. In the absence of AA, no redox peaks were observed, confirming that the developed nanosensor is electrochemically stable under the experimental conditions and does not undergo spontaneous oxidation or reduction (Fig. 4a). Fig. 4b demonstrates a comparison of the sensitivity performance of the developed sensors, $Ag_{0.02}Cu_{0.98}Fe_2O_4$-CPE and $Ag_{0.02}Cu_{0.98}Fe_2O_4$@-chitosan-CPE, with the bare CP electrode in detecting AA. When 5 mM AA was added to the cell, a very slight current response was observed on the bare CPE surface, which was somewhat enhanced in the synthesized $Ag_{0.02}Cu_{0.98}Fe_2O_4$-CPE. Interestingly, the $Ag_{0.02}Cu_{0.98}Fe_2O_4$@chitosan-CPE polymerized nanosensor exhibited a sharp redox peak for ascorbic acid, confirming its superior efficacy. Specifically, a pronounced anodic peak appeared at +0.28 V with a catalytic current of 432 μA, compared to a less defined anodic peak at +0.55 V. Scheme 2

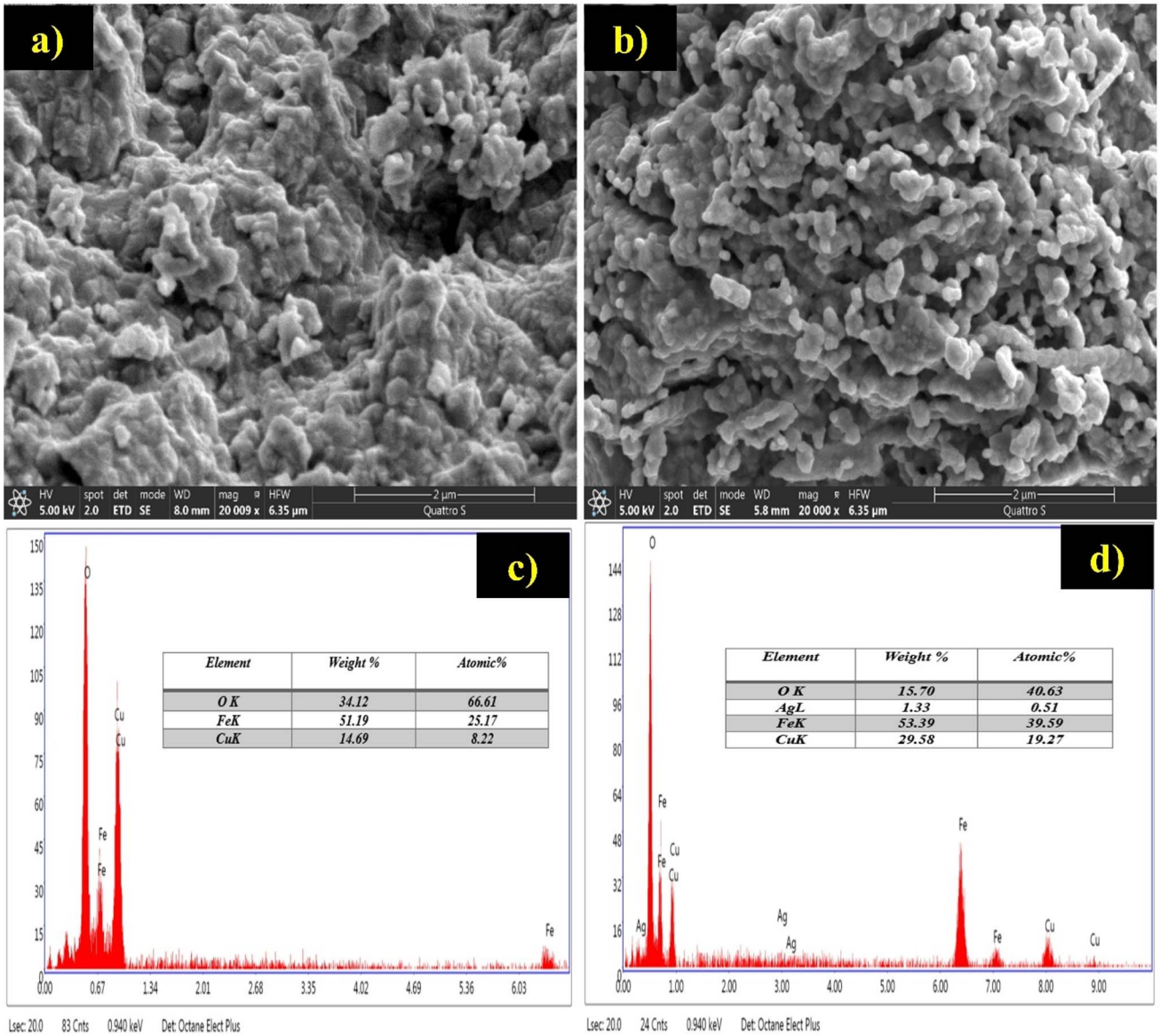

Fig. 3 SEM-EDX analysis of: pure $CuFe_2O_4$ NPs (a and c), and doped $Ag_{0.02}Cu_{0.98}Fe_2O_4$ nanostructured (b and d).

illustrates the electrochemical oxidation mechanism of ascorbic acid on the fabricated electrode surface. It was observed to be oxidized to dehydroascorbic acid (DHA).[61] Indeed, the absence of a corresponding reduction peak after the electro-oxidation peak in the CVs of AA indicates that the oxidized product (DHA) is not electro-reduced back to AA under the experimental conditions, suggesting that the oxidation process is irreversible.

These findings demonstrate the superior electrocatalytic performance of the $Ag_{0.02}Cu_{0.98}Fe_2O_4$@chitosan-modified electrode toward AA oxidation, attributed to the synergistic interaction between the nanocomposite and the chitosan matrix, which contributes to enhance electron transfer and improved conductivity of the sensor surface.[62–64]

3.2.1 Scan rate impact. It is used to further examine the electrochemical mechanism of the engineered chitosan-based nano-sensor. As shown in Fig. 5a, increasing the scan rate (from 25 to 200 mV s^{-1}) caused the anodic peak potential to shift to more positive values. This was accompanied by a proportional increase in the anodic peak current (I_{pa}). Interestingly, the anodic peak current scaled linearly with the square root of the scan rate ($\nu^{1/2}$) and with a high coefficient of determination ($R^2 = 0.9895$), as depicted in in Fig. 5b. These results confirm that the electrocatalytic oxidation is controlled primarily by the analyte's (AA) diffusion from the solution to the electrode ($Ag_{0.02}Cu_{0.98}Fe_2O_4$@chitosan-CPE) surface under the tested conditions.[65–67]

Fig. 5c shows a graph of the logarithm of the anodic peak current (I_{pa}) and the logarithm of the scan rate (ν). A straight line with a slope of 0.3734 is obtained, confirming that the process is indeed under diffusion control, as this line deviates slightly from the theoretical value of 0.5 for such a process.[68] Furthermore, Laveron's formula (eqn (11)) was applied to determine the electron transfer coefficient (α) and the number of electrons (n) involved in the redox process.[68]

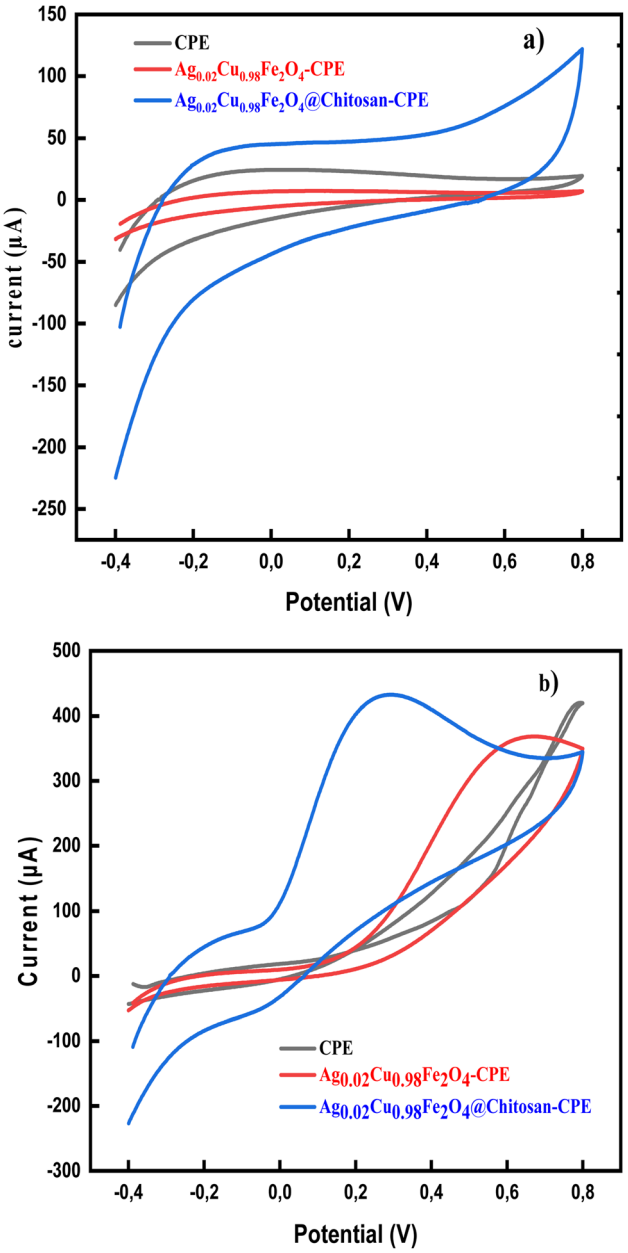

Fig. 4 Cyclic voltammograms acquired on the CPE, $Ag_{0.02}Cu_{0.98}Fe_2O_4$-CPE and $Ag_{0.02}Cu_{0.98}Fe_2O_4$@chitosan-CPE at 50 mV s^{-1} sweep rate in: PBS solution (pH = 7.0) without AA (a), and the existence of AA, 5 mM (b).

$$E_{pa} = E_0(RT/\alpha nF) + \ln(RTk/\alpha nF) + (RT/\alpha nF)\ln v \quad (11)$$

where $R = 8.314$ J K^{-1} mol^{-1}, $F = 96485$C mol^{-1}, and $T = 298$ K. The slope (m) of the linear plot of the anodic peak potential (E_{pa}) *versus* $\ln(v)$ as shown in Fig. 5d, corresponds to the term $RT/\alpha nF$. Therefore, the value of α can be found from experimental measurements as follows:

$$\alpha = RT/mnF \quad (12)$$

For a process involving $n = 2$ (Scheme 2) and $m = 0.05392$ V, the value of α was estimated to be 0.2381.

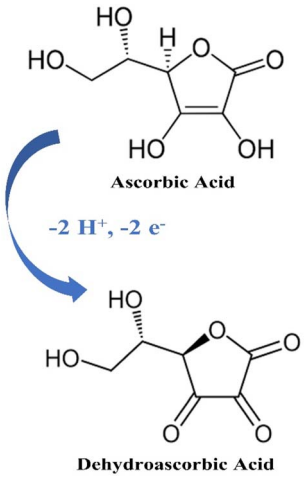

Scheme 2 AA electrochemical oxidation mechanism.

The diffusion coefficient (D) for AA was calculated using the Randles–Ševcik equation:[69]

$$I_{pa} = 2.69 \times 10^5\, n^{(3/2)}\, D^{(1/2)}\, AC\, v^{(1/2)} \quad (13)$$

I_{pa} = Peak current (A), C = AA concentration (mol cm^{-3}), A = electrode surface area (cm^2). The value of D was then calculated to be 1.06×10^{-6} cm^2 s^{-1}.

3.2.2 Effect of concentration. To further evaluate the performance of the designed sensor, the effect of varying AA concentrations was examined. Using different doses of AA (100 μM to 13 mM) in 0.1 M PBS solution, where the sensitivity, linearity response window, and LOD of the newly synthesized ferrite NPs functionalized with chitosan-modified CPE were determined. The detection limit was estimated as follows: LOD = $3\sigma/m$, (σ = standard deviation of blank signal and m = slope of calibration curve, expressing sensitivity). As illustrated in Fig. 6a, the oxidation peak current of AA increased linearly, while the oxidation peak potential shifted to a more positive outlook, with increasing AA concentration. This strong linear relationship ($R^2 \approx 1$) depicted in the calibration curve (Fig. 6b), indicates that the sensor is highly effective and suitable for quantifying the analyte (AA) across a broad range (from 100 μM to 13 mM). The sensor exhibited two distinct linear ranges, each with its own sensitivity: (i) 411.59 μA mM^{-1} cm^2 in the range of 100–300 μM (lower concentration range), and (ii) 327.31 μA mM^{-1} cm^2 in the range of 300 μM–13 mM (higher concentration range).The LOD of the sensor was found to be 89 μM, highlighting its excellent sensitivity and suitability for trace-level AA detection. To further validate its performance, Table 1 compares the results of this sensor with previously reported electrodes for vitamin C detection.

3.2.3 Reproducibly/repeatability/stability. To further confirm the performance of the designed sensor, its stability and repeatability were systematically examined. Three $Ag_{0\cdot02}$-$Cu_{0\cdot98}Fe_2O_4$@chitosan-modified CPE electrodes, fabricated under identical conditions, were employed to detect 5 mM AA in 0.1 M PBS using the CV technique. In addition, one electrode was subjected to 15 consecutive measurements of AA (5 mM) to

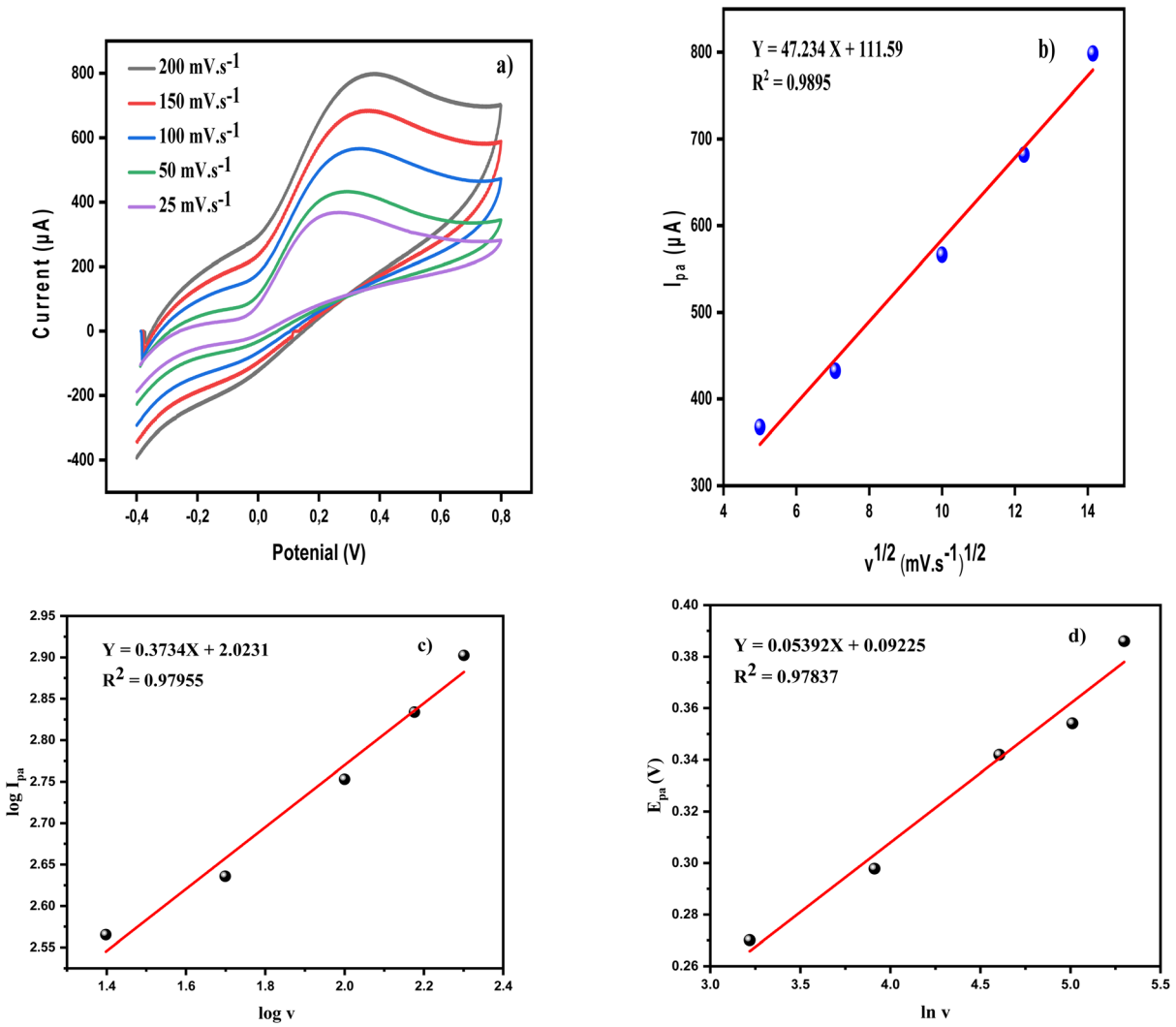

Fig. 5 (a) CV curves of $Ag_{0.02}Cu_{0.98}Fe_2O_4$@chitosan-CPE in PBS solution (0.1 M) containing 5 mM of AA at different scan rates (25 to 200 mV s^{-1}), (b) correlation of I_{pa} and the $\nu^{1/2}$. (c) A graph of the log(I_{pa}) *vs.* log(ν), and (d) the linear plot of the anodic peak potential (E_{pa}) *vs.* ln(ν).

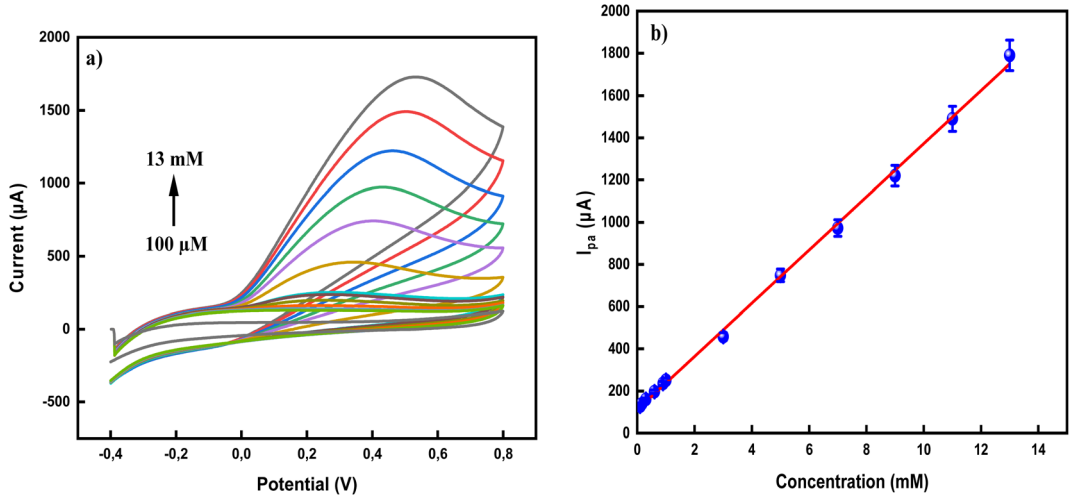

Fig. 6 (a) CVs of $Ag_{0.02}Cu_{0.98}Fe_2O_4$@chitosan-CPE recorded at various concentrations of AA (100 µM to 13 mM) in 0.1 M PBS solution, (b) calibration curve (with error bars) of anodic peak current (I_{pa}) *vs.* AA concentration.

Table 1 Comparing the performance of different electrodes with the new modified chitosan-based sensor towards AA detection[a]

Electrode	Technique	LOD (μM)	Linear range (μM)	Ref.
MWCNT-AONP@SPCE	SWV	0.14	0.04–0.64	70
CF/ZnO CN-ME	DPV	156.7	0.6–1800	71
Pd-PPy/Si	CV	200	500–10000	72
(Ag/CNT-CPE)	DPV	12	30–2000	16
Graphite screen printed electrode modified with $NiFe_2O_4$NPs	DPV	0.1	0.5–100.0	17
$Ag_{0.02}Cu_{0.98}Fe_2O_4$@chitosan-CPE	CV	89	100–300 300–13000	This work

[a] DPV = differential pulse voltammetry, and SWV = square wave voltammetry.

evaluate repeatability. The results showed relative standard deviations (RSD%) of 1.96% for reproducibility and 1.15% for repeatability. These low RSD values confirm the excellent stability and reliability of the $Ag_{0.02}Cu_{0.98}Fe_2O_4$@chitosan-CPE sensor during the AA detection process, highlighting its robustness for practical applications. The long-term stability of $Ag_{0\cdot02}Cu_{0\cdot98}Fe_2O_4$@chitosan-modified CPE was also evaluated by measuring its current response after one week under ambient conditions. The oxidation peak current retained 95.06% of its initial value, demonstrating the good long-term stability of the electrode.[73]

3.2.4 Interferences. Selectivity is a critical parameter in defining the effectiveness of electrochemical sensors. To ensure accuracy and selectivity, the designed $Ag_{0\cdot02}Cu_{0\cdot98}Fe_2O_4$@chitosan-CPE sensor response was evaluated in the existence of other chemicals that might interfere with AA signal during an electro-oxidation process. For this purpose, the electro-analytical response of the sensor towards a very low concentration of AA (0.5 mM) in the presence of different potential interferents (interf), each at a higher concentration (50 mM) such as glucose (GL), fructose (Fr), sucrose (Suc), KCl, and NaCl, all prepared in 0.1 M PBS, was investigated (Fig. 7). Surpassingly, findings demonstrated that these interfering species produced no significant effect on the oxidation current of AA, thereby confirming the excellent selectivity and strong anti-interference capability of the $Ag_{0\cdot02}Cu_{0\cdot98}Fe_2O_4$@chitosan-modified sensor system.[74,75]

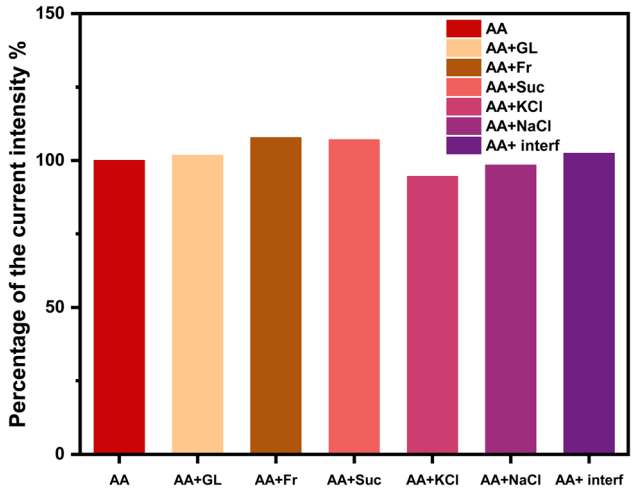

Fig. 7 Selectivity evaluation of AA (0.5 mM) in the existence of 50 mM of different potential interferents.

3.2.5 Real sample applications. In a real-world example, the new sensor was used to identify and quantify the target analyte (AA) in complex environments. Therefore, two different samples of orange juice, natural and commercial, were examined to accurately assess the sensor's performance. This application step verifies the effectiveness, capability, selectivity, and accuracy of the developed nanosensor despite the presence of other interfering components, ensuring its reliability and usefulness outside of a controlled laboratory environment. Prior to electrochemical measurements, the samples were centrifuged for 15 min to remove the pulp and suspended solids, followed by filtration process, and appropriately diluted with phosphate buffer solution (PBS, 0.1 M, pH 7.0) at a dilution ratio of 1 : 10 (v/v) to reduce matrix effects. To minimize matrix effects from sugars, organic acids, and other electroactive compounds commonly preset in orange juice, the quantification was performed using the standard addition method, which is considered a reliable strategy for compensating matrix effects in electrochemical measurements. Recovery studies were carried out by spiking know concentration of AA into the

Table 2 Determining AA in real beverage samples

Orange juice sample	Added concentration (mM)	Measured concentration (mM)	Recovery (%)
Natural	0.15	0.147	98.0
	0.50	0.490	98.0
	1.0	0.979	97.9
Commercial	0.15	0.146	97.3
	0.50	0.487	97.4
	1.0	0.974	97.4

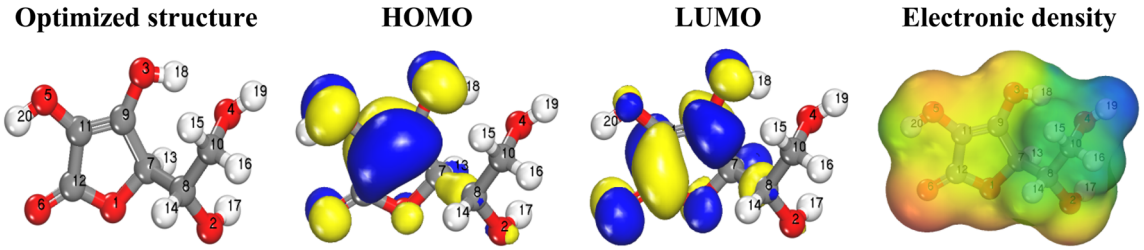

Fig. 8 Optimized structure, (HOMO, LUOMO) distribution and MESP map of AA.

Table 3 Ascorbic acid computed descriptors

Area (Å^2)	Volume (Å^3)	E_{LUMO} (eV)	E_{HOMO} (eV)	ΔE_{gap} (eV)	A (eV)	I (eV)	χ (eV)	σ (eV^{-1})	η (eV)
177.00	169.13	−1.09	−6.51	5.42	6.51	1.09	3.800	0.369	2.710

pretreated samples, and all measurement were performed in triplicate.[76]

As summarized in Table 2, the new sensor achieved good recovery rate of 97–98%. This signifies high accuracy and efficiency, as only a very small percentage of the target analyte was lost or interfered with by the complex components of the orange juice matrix during the detection process.[77,78] Since the current modified electrode can now be efficiently applied to measure AA in real-world samples, this highlights the success of the modification process in overcoming the limitations of bare electrodes, *e.g.*, CPE, and thus may contribute to a future industrial renaissance.

3.3 Computational explorations

3.3.1 DFT calculations. The geometric and electronic descriptors calculated from the AA optimized structure (Fig. 8) have been listed in Table 3. The moderate value of (ΔE_{gap}) and volume area of AA confirm its reactivity and receptivity. The reactivity of this molecule has been proved by its high softness value and low hardness value.

Optimized structure, frontier molecular orbitals (HOMO and LUOMO) distribution and MESP map of AA have been depicted in Fig. 8. As it appears, the HOMO and LUMO orbitals are extended over the cyclic part and their attached hydroxyl and carbonyl groups of AA molecule, indicating the reactivity of these parts.

MESP analyses map the electron density around the surface of a molecule, revealing regions of positive and negative potentials to identify reactive sites, predict interactions, and understand molecular behavior. Noteworthy, this visual tool helps to locate the nucleophilic (electron-rich) or electrophilic (electron-poor) attack.[79] This is achieved by mapping the electrostatic potential onto the molecular surface using a color code: red regions correspond to areas of high electron density and strong negative potential, indicating likely sites for electrophilic attack, while blue regions represent electron-deficient zones with positive potential, prone to nucleophilic attack; intermediate potentials are shown in green. In the case of AA, MESP mapping reveals that the oxygen atoms (especially O6) exhibit pronounced negative potential (red), highlighting them as key active sites for electrophilic interactions, whereas the hydrogen atom of the alcohol group (H19) displays a positive potential (blue), marking it as a nucleophilic site. This spatial distribution of electrostatic potential not only clarifies the molecule's reactive hotspots but also informs on its interaction tendencies in various chemical environments, thereby underpinning mechanistic insights into its chemical behavior and reactivity.[80,81]

3.3.2 Local descriptors (Fuckui indices, FIs). The FIs are significant indicators for evaluating the most reactive atoms within a molecule. These indices help predict whether a molecule acts as an electron donor, an electron acceptor, or both. In this context, the FIs of AA (f^-, f^+, and f^0) have been evaluated.

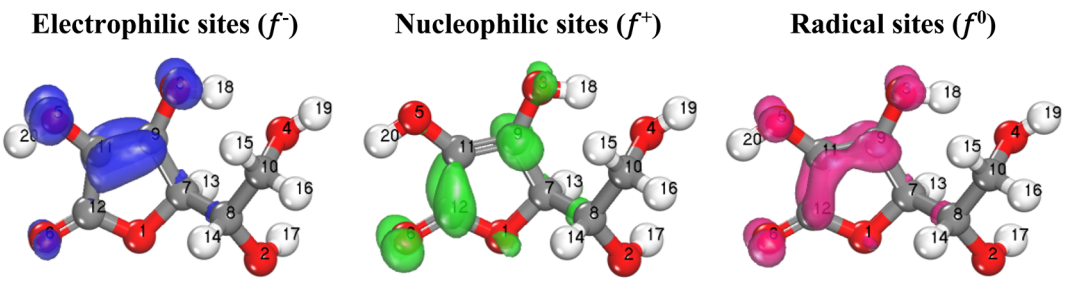

Fig. 9 Iso surfaces of the electrophilic, nucleophilicand radical FIs of AA.

Table 4 FIs of AA

Atom N°	f^-	f^+	f^0	Atom N°	f^-	f^+	f^0
O1	0.046	0.074	0.060	C11	0.152	0.083	0.118
O2	0.019	0.019	0.019	C12	0.052	0.162	0.107
O3	0.132	0.086	0.109	H13	0.033	0.051	0.042
O4	0.006	0.006	0.006	H14	0.013	0.015	0.014
O5	0.167	0.055	0.111	H15	0.007	0.008	0.008
O6	0.097	0.177	0.137	H16	0.010	0.012	0.011
C7	0.022	0.027	0.024	H17	0.008	0.011	0.010
C8	0.011	0.015	0.013	H18	0.034	0.025	0.030
C9	0.124	0.134	0.129	H19	0.008	0.008	0.008
C10	0.004	0.006	0.005	H20	0.054	0.027	0.040

Their distributions are illustrated in the Fig. 9, and their quantitative values are listed in the Table 4.

The FIs results (Table 4) show that the atoms most susceptible to electrophilic attacks (acting as electron donors) are O5 and C11, due to their highest values of f^-. Conversely, the atoms most susceptible to nucleophilic attacks (acting as electron acceptors) are O6 and C12, owing to their highest values of f^+. It is also observed that these same atoms exhibit the highest values of f^0, indicating that they are the most sensitive to radical attacks.[82]

Generally, the three FIs are distributed on the studied molecule's cyclic part and their attached hydroxyl and carbonyl groups, indicating that these parts are the most susceptible for electrophilic and nucleophilic attacks therefore they are responsible for electronic exchange.[83–85]

Table 5 Conformational search parameters of chitosan and AA

Parameters	Chitosan	AA
Average energy(kcal mol^{-1})	123.111	28.398
Average RMSD (Å)	0.168	0.327
Minimum energy (kcal mol^{-1})	123.105	28.397
N° of torsion angles	13	2

3.3.3 MCS simulation. Initially, the most stable structures of chitosan and AA molecules were determined by conformational analysis using the Conformers option in Materials Studio 2017, combining the random sampling method with the Universal Force Field. The lowest-energy structures of chitosan and AA, along with the conformer search results (1000 conformers), are shown illustrated Fig. 10, while the conformational search parameters are summarized in Table 5.

Analysis of the findings in Table 5 confirms that AA is the most stable compound than Chitosan due to its lowest energy and torsion angles values. MC simulations were applied to investigating the adsorption behavior of ascorbic acid (AA) on three distinct carbon paste electrode (unmodified CPE, $Ag_{0.02}$-$Cu_{0.98}Fe_2O_4$-modified CPE, and $Ag_{0.02}Cu_{0.98}Fe_2O_4$@chitosan-modified CPE) systems under conditions mimicking experimental setups. The graphite (CPE) model consisted of a box formed by two carbon sheets oriented along the (001)

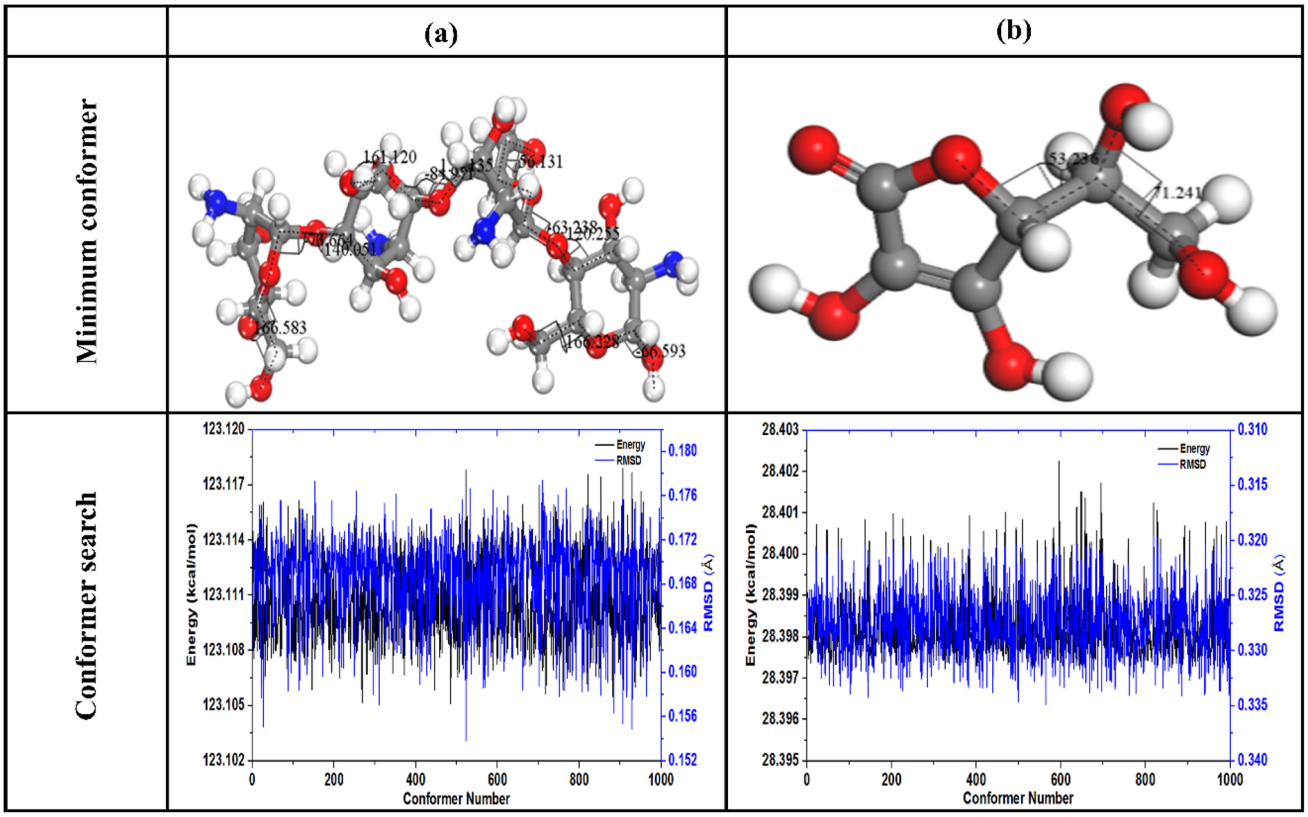

Fig. 10 Conformational search of (a) chitosan and (b) AA.

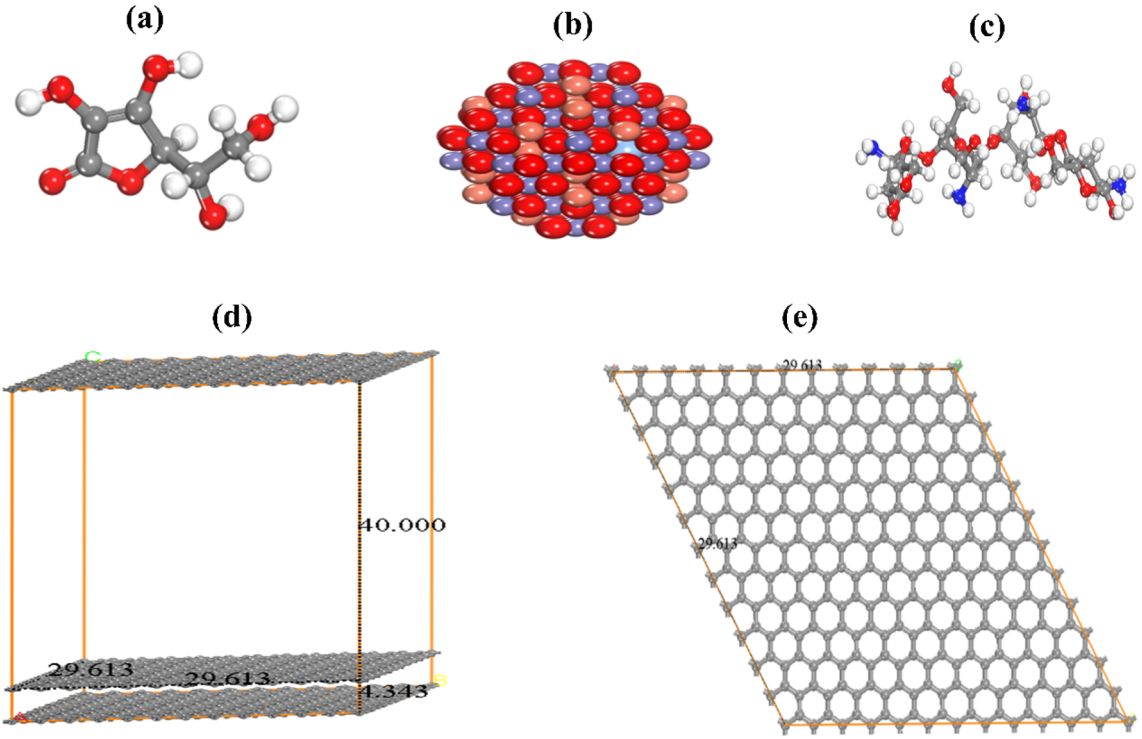

Fig. 11 Initial structures used in the MC simulation (a) AA, (b) $Ag_{0.02}Cu_{0.98}Fe_2O_4$cluster and (c) chitosan. (d) Side view of a two-dimensional graphite box composed of two carbon sheets oriented in the (001) direction and (e) a top view of a single graphite layer (with dimensions).

crystallographic plane. The initial structures of AA, chitosan molecules, and the $Ag_{0.02}$ $Cu_{0.98}$ Fe_2O_4 cluster used in the simulations, along with top and side views of the two-dimensional graphite box, are depicted in Fig. 11.

This work utilized three surface configurations for analysis. The first (AA-CPE) have been constructed by packing one molecule AA on graphite surface, the second have been built by packing one molecule AA on ($Ag_{0.02}Cu_{0.98}Fe_2O_4$cluster + graphite surface) system and the third have been constructed by packing one molecule AA on ($Ag_{0.02}Cu_{0.98}Fe_2O_4$cluster + two Chitosan unit + graphite surface) system. In the last case, the AA structure has been highlighted in yellow to make it easier to distinguish from other structures. The interaction between AA and each electrode systems is quantified by Adsorbate–substrate systems' adsorption energy (E_{ads}). Therefore, macroscopic results from electrochemical measurements can be systematically compared with microscopic insights from Monte Carlo (MC) simulations to bridge experimental observations with atomic-scale mechanisms in the three electrode systems.

All calculated adsorption energies (E_{ads}) were negative, unequivocally demonstrating that the interaction between the AA molecule and the various electrode surfaces is both spontaneous and strongly attractive. Among the electrodes studied, the $Ag_{0.02}Cu_{0.98}Fe_2O_4$-functionalized chitosan-modified carbon paste electrode ($Ag_{0.02}Cu_{0.98}Fe_2O_4$@chitosan-CPE) exhibited a notably higher adsorption energy magnitude of -26.65 kcal mol^{-1} compared to other electrodes (Fig. 12). This substantial adsorption energy indicates significantly enhanced electrostatic interactions and superior stabilization of the AA molecule on the electrode surface. The presence of nanoclusters functionalized chitosan not only provides abundant active sites but also promotes favorable hydrogen bonding and electrostatic attractions, which collectively strengthen the adsorbate–substrate complex. Such pronounced binding affinity highlights the critical role of chitosan modification in optimizing the electrode interface, thereby facilitating more efficient molecular adsorption. This enhancement directly translates to improved electrocatalytic activity and sensitivity of the sensor, making the $Ag_{0.02}$ $Cu_{0.98}$ Fe_2O_4@chitosan-CPE system particularly effective for the selective and robust detection of AA in electrochemical applications. These atomic-level findings, in good agreement with macroscopic electrochemical results.

The adsorption energy distribution profiles obtained from the MC simulations (Fig. 13) provide valuable insights into the strength and uniformity of AA adsorption on the three investigated electrode surfaces: AA/CPE, AA/$Ag_{0.02}Cu_{0.98}Fe_2O_4$-CPE, and AA/$Ag_{0.02}Cu_{0.98}Fe_2O_4$@chitosan-CPE. In these simulations, the adsorption energy (E_{ads}) reflects the total energy change accompanying the adsorption process, with more negative values indicating stronger interactions and greater stability of the AA-metal surface system; however, a high sensitivity of detection is observed. The results clearly show that the energy distributions of the AA/$Ag_{0.02}Cu_{0.98}Fe_2O_4$@chitosan-CPE electrode shifted towards more negative energy values compared to the other two electrodes, indicating its high sensitive detection. This behavior suggests that the chitosan-modified electrode surface provides a higher density of active sites, improving the adsorption affinity and uniformity of AA/electrode binding[74,75]

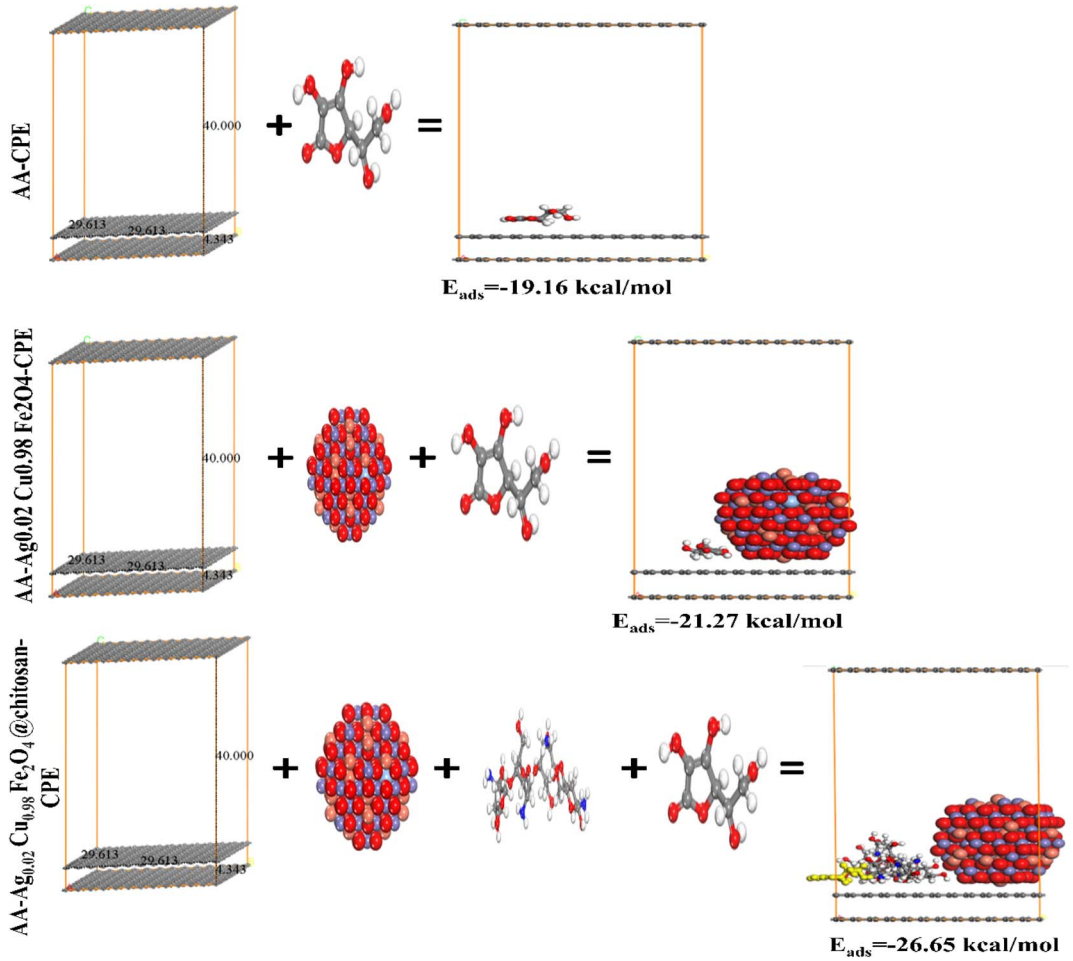

Fig. 12 Optimal adsorption sites and their adsorption energies (E_{ads}).

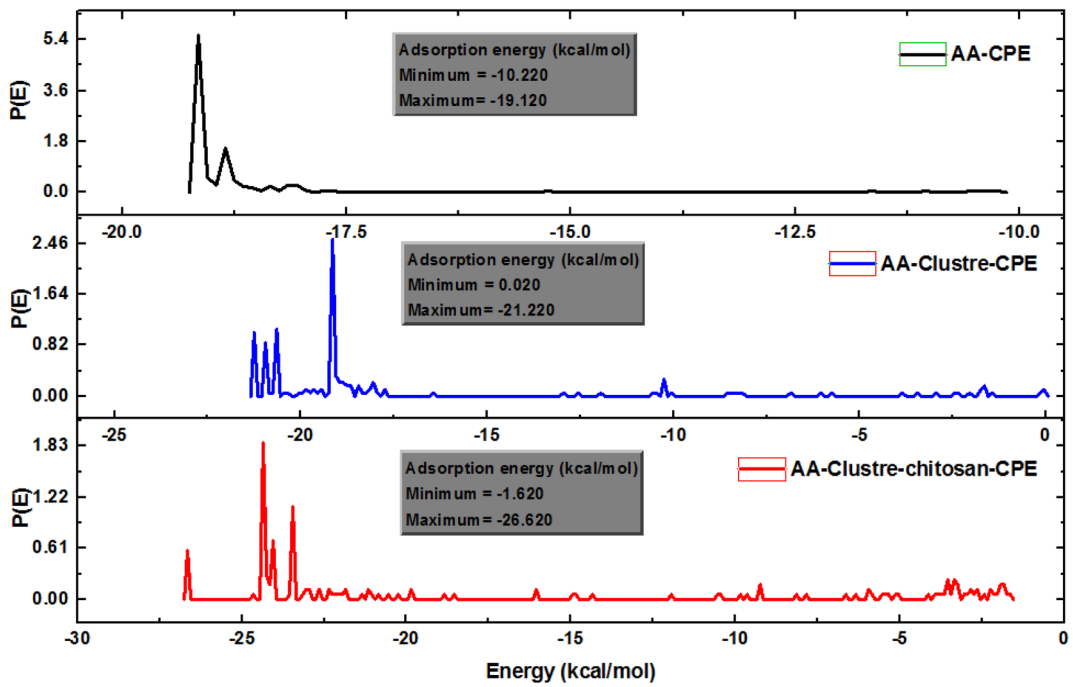

Fig. 13 Adsorption energy distributions of AA on the three electrodes examined during MC simulation.

4 Conclusions

In this investigation, a high-performance electrochemical sensor based on $Ag_{0.02}Cu_{0.98}Fe_2O_4$NPs functionalized with chitosan for the effective detection of AA is effectively fabricated and characterized. Structural (XRD) and vibrational (FTIR) evaluations confirmed the effective integration of chitosan, which significantly enhanced the material's physicochemical properties. SEM and EDX were also used to analyze the surface morphology and elemental composition of the designed nanostructured. The electrochemical tests revealed that the $Ag_{0.02}Cu_{0.98}Fe_2O_4$@chitosan-CPE exhibited a remarkable shift in oxidation potential from +0.55 V to +0.28 V, along with an improved current response of 432 μA, indicating excellent electrocatalytic activity. A wide dynamic range was observed, consisting of two linear segments between 100–300 μM and 300 μM–13 mM, with high sensitivities of 411.59 μA mM^{-1} cm^2 and 327.31 μA mM^{-1} cm^2, respectively. The LOD was estimated to be 89 μM, placing this sensor among the most efficient systems reported in recent literature. The sensor showed excellent stability (RSD = 1.15%), reproducibility (RSD = 1.96%), and anti-interference capacity, even when typical interferents are present in significant amounts. The designed sensor has proven to be an accurate, sensitive, selective, and reliable method for measuring AA in a real-world environment. Theoretical investigations using DFT highlighted the reactive nature of AA, particularly at oxygen-rich sites, supported by FIs and MESP analyses. Furthermore, Monte Carlo simulations revealed notably high adsorption energy of −26.65 kcal mol^{-1} for AA on the modified electrode, underscoring the strong binding interactions and synergistic effect of the chitosan functionalized nanomaterial. Altogether, the integration of $Ag_{0.02}Cu_{0.98}Fe_2O_4$ NPs with chitosan not only improved the electrochemical performance but also provided theoretical validation for enhanced molecular interactions, thereby offeringa powerful, selective, and sensitive platform for real-time detection of biologically important molecules such as AA. Future work may focus on extending this approach to detect other electroactive biomolecules and integrating the sensor into portable devices for field applications.

Conflicts of interest

There are no conflicts to declare.

Data availability

Data will be available at request.

Acknowledgements

This work was supported and funded by the Deanship of Scientific Research at Imam Mohammad Ibn Saud Islamic University (IMSIU) (grant number IMSIU-DDRSP2602).

References

1 C. Lakshmi Devi and S. Sriman Narayanan, Poly(amido amine) dendrimer and silver nanoparticle–multi-walled carbon nanotubes composite with poly(neutral red)-modified electrode for the determination of ascorbic acid, *Bull. Mater. Sci.*, 2019, **42**(42), 1–11, DOI: 10.1007/S12034-019-1775-7.

2 D. Huang, X. Li, M. Chen, F. Chen, Z. Wan, R. Rui, R. Wang, S. Fan and H. Wu, An electrochemical sensor based on a porphyrin dye-functionalized multi-walled carbon nanotubes hybrid for the sensitive determination of ascorbic acid, *J. Electroanal. Chem.*, 2019, **841**, 101–106, DOI: 10.1016/J.JELECHEM.2019.04.041.

3 Y. Ma, Y. Zhang and L. Wang, An electrochemical sensor based on the modification of platinum nanoparticles and ZIF-8 membrane for the detection of ascorbic acid, *Talanta*, 2021, **226**, 122105, DOI: 10.1016/J.TALANTA.2021.122105.

4 Z. N. Huang, J. Zou, J. Teng, Q. Liu, M. M. Yuan, F. P. Jiao, X. Y. Jiang and J. G. Yu, A novel electrochemical sensor based on self-assembled platinum nanochains - Multi-walled carbon nanotubes-graphene nanoparticles composite for simultaneous determination of dopamine and ascorbic acid, *Ecotoxicol. Environ. Saf.*, 2019, **172**, 167–175, DOI: 10.1016/J.ECOENV.2019.01.091.

5 A. Pardakhty, S. Ahmadzadeh, S. Avazpour and V. K. Gupta, Highly sensitive and efficient voltammetric determination of ascorbic acid in food and pharmaceutical samples from aqueous solutions based on nanostructure carbon paste electrode as a sensor, *J. Mol. Liq.*, 2016, **216**, 387–391, DOI: 10.1016/J.MOLLIQ.2016.01.010.

6 S. Sharifian and A. Nezamzadeh-Ejhieh, Modification of carbon paste electrode with Fe(III)-clinoptilolitenanoparticles for simultaneous voltammetric determination of acetaminophen and ascorbic acid, *Mater. Sci. Eng. C*, 2016, **58**, 510–520, DOI: 10.1016/J.MSEC.2015.08.071.

7 W. Liao, C. Guo, L. Sun, Z. Li, L. Tian, J. He, J. Li, J. Zheng, Z. Ma, Z. Luo and C. Chen, The Electrochemical Behavior of Nafion/Reduced Graphene Oxide Modified Carbon Electrode Surface and Its Application To Ascorbic Acid Determination, *Int. J. Electrochem. Sci.*, 2015, **10**, 5747–5755, DOI: 10.1016/S1452-3981(23)17292-0.

8 Z. M. Khoshhesab, Simultaneous electrochemical determination of acetaminophen, caffeine and ascorbic acid using a new electrochemical sensor based on CuO–graphenenanocomposite, *RSC Adv.*, 2015, **5**, 95140–95148, DOI: 10.1039/C5RA14138A.

9 B. Bharali, P. Bordoloi and D. K. Das, Condensation product of 5-bromosalicylaldehyde and aminophenol: Fluorescence sensor for ascorbic acid and AND Logic Gate, *Indian J. Chem.*, 2022, **61**, 497–502, DOI: 10.56042/ijc.v61i5.63640.

10 Z. Y. SONG, Y. MA and J. S. YE, Electrochemical Sensors for Simultaneous Determination of Small Biomolecules By 3D Layered Hollow Honeycomb-like Ni-NiO@CPVP Modified Glassy Carbon Electrode, *Chin. J. Anal. Chem.*, 2020, **48**, e20047–e20055, DOI: 10.1016/S1872-2040(20)60010-X.

11 T. Dimitrijević, P. Vulić, D. Manojlović, A. S. Nikolić and D. M. Stanković, Amperometric ascorbic acid sensor based on doped ferrites nanoparticles modified glassy carbon paste electrode, *Anal. Biochem.*, 2016, **504**, 20–26, DOI: 10.1016/J.AB.2016.03.020.

12 S. M. Siddeeg, N. S. Alsaiari, M. A. Tahoon and F. Ben Rebah, The Application of Nanomaterials as Electrode Modifiers for the Electrochemical Detection of Ascorbic Acid: Review, *Int. J. Electrochem. Sci.*, 2020, **15**, 3327–3346, DOI: 10.20964/2020.04.13.

13 X. Zhang, S. Yu, W. He, H. Uyama, Q. Xie, L. Zhang and F. Yang, Electrochemical sensor based on carbon-supported NiCoO2 nanoparticles for selective detection of ascorbic acid, *Biosens. Bioelectron.*, 2014, **55**, 446–451, DOI: 10.1016/J.BIOS.2013.12.046.

14 J. Song, L. Xu, R. Xing, Q. Li, C. Zhou, D. Liu and H. Song, Synthesis of au/graphene oxide composites for selective and sensitive electrochemical detection of ascorbic acid, *Sci. Rep.*, 2014, **4**, 1–7, DOI: 10.1038/SREP07515.

15 C. L. Sun, H. H. Lee, J. M. Yang and C. C. Wu, The simultaneous electrochemical detection of ascorbic acid, dopamine, and uric acid using graphene/size-selected Pt nanocomposites, *Biosens. Bioelectron.*, 2011, **26**(8), 3450–3455, DOI: 10.1016/j.bios.2011.01.023.

16 J. Tashkhourian, M. H. Nezhad, J. Khodavesi and S. Javadi, Silver nanoparticles modified carbon nanotube paste electrode for simultaneous determination of dopamine and ascorbic acid, *J. Electroanal. Chem.*, 2009, **633**(1), 85–91, DOI: 10.1016/j.jelechem.2009.04.028.

17 H. D. Madhuchandra, B. E. Kumara Swamy and T. S. Sunil Kumar Naik, Pretreated carbon paste electrode sensor for Adrenaline: A voltammetric study, *Chem. Data Collect.*, 2020, **28**, 100388, DOI: 10.1016/j.cdc.2020.100388.

18 H. F. Assaf, H. Salah, N. Hashem, M. Khodari and A. Toghan, Fabrication of an electrochemical sensor based on copper waste wire recycling and its application, *Sensor Actuator Phys.*, 2021, **331**, 112962, DOI: 10.1016/j.sna.2021.112962.

19 A. Toghan, M. Abd-Elsabour and A. M. Abo-Bakr, A novel electrochemical sensor based on EDTA-NQS/GC for simultaneous determination of heavy metals, *Sensor Actuator Phys.*, 2021, **322**, 112603, DOI: 10.1016/j.sna.2021.112603.

20 M. S. Mohammadnia, E. M. Khosrowshahi, E. Naghian, A. H. Keihan, E. Sohouli, M. E. Plonska-Brzezinska, A. Sobhani-Nasab, M. Rahimi-Nasrabadi and F. Ahmadi, Application of carbon nanoonion-NiMoO4-MnWO4 nanocomposite for modification of glassy carbon electrode: Electrochemical determination of ascorbic acid, *Microchem. J.*, 2020, **159**, 105470, DOI: 10.1016/J.MICROC.2020.105470.

21 W. Boultif, C. Dehchar, Y. Belhocine, E. Zouaoui, S. Rahali, S. E. Zouari, N. Sbei and M. Seydou, Chitosan and Metal Oxide Functionalized Chitosan as Efficient Sensors for Lead (II) Detection in Wastewater, *Separations*, 2023, **10**, 479, DOI: 10.3390/SEPARATIONS10090479.

22 M. A. Ahmed, M. A. Ahmed and A. A. Mohamed, Synthesis, characterization and application of chitosan/graphene oxide/copper ferrite nanocomposite for the adsorptive removal of anionic and cationic dyes from wastewater, *RSC Adv.*, 2023, **13**, 5337–5352, DOI: 10.1039/D2RA07883J.

23 H. N. Abdelhamid and H. F. Wu, Facile synthesis of nano silver ferrite (AgFeO2) modified with chitosan applied for biothiol separation, *Mater. Sci. Eng. C*, 2014, **45**, 438–445, DOI: 10.1016/J.MSEC.2014.08.071.

24 A. Toghan, N. Roushdy, S. A. Al-Hussain, M. S. Elnouby, S. M. Yousef, A. A. M. Farag, M. E. Youssef and N. A. Elessawy, Assessing the performance of novel and sustainable electrochemical sensor based on cobalt sulfide/upcycled reduced graphene oxide from plastic waste, *Electrochem. Commun.*, 2025, **177**, 107982, DOI: 10.1016/j.elecom.2025.107982.

25 F. P. de Freitas, A. M. M. L. Carvalho, A. de C. O. Carneiro, M. A. de Magalhães, M. F. Xisto and W. D. Canal, Adsorption of neutral red dye by chitosan and activated carbon composite films, *Heliyon*, 2021, **7**(7), e07629, DOI: 10.1016/j.heliyon.2021.e07629.

26 S. Shiri, N. Pajouheshpoor, H. Khoshsafar, S. Amidi and H. Bagheri, An electrochemical sensor for the simultaneous determination of rifampicin and isoniazid using a C-dots@CuFe2O4 nanocomposite modified carbon paste electrode, *New J. Chem.*, 2017, **41**, 15564–15573, DOI: 10.1039/C7NJ03029K.

27 R. Ramadan and M. M. El-Masry, Effect of (Co and Zn) doping on structural, characterization and the heavy metal removal efficiency of CuFe2O4 nanoparticles, *J. Australas. Ceram. Soc.*, 2024, **60**, 509–524, DOI: 10.1007/S41779-023-00932-5/TABLES/6.

28 P. M. Jahani, M. Jafari and F. N. Ravari, CuFe2O4 nanoparticles-based electrochemical sensor for sensitive determination of the anticancer drug 5-fluorouracil, *ADMET DMPK*, 2023, **11**(2), 201–210, DOI: 10.5599/admet.1691.

29 M. E.-S. Abdel-Raouf, R. K. Farag, A. A. Farag, M. Keshawy, A. Abdel-Aziz and A. Hasan, Chitosan-Based Architectures as an Effective Approach for the Removal of Some Toxic Species from Aqueous Media, *ACS Omega*, 2023, **8**, 10086–10099, DOI: 10.1021/acsomega.2c07264.

30 B. Wang, S. Gu, Y. Ding, Y. Chu, Z. Zhang, X. Ba, Q. Zhang and X. Li, A novel route to prepare LaNiO 3 perovskite-type oxide nanofibers by electrospinning for glucose and hydrogen peroxide sensing, *Analyst*, 2012, **138**, 362–367, DOI: 10.1039/C2AN35989H.

31 T. W. Chen, S. Chinnapaiyan, S. M. Chen, M. Ajmal Ali, M. S. Elshikh and A. Hossam Mahmoud, Facile synthesis of copper ferrite nanoparticles with chitosan composite for high-performance electrochemical sensor, *Ultrason. Sonochem.*, 2020, **63**, 104902, DOI: 10.1016/J.ULTSONCH.2019.104902.

32 S. Pitakrut, P. Sanchayanukun, C. Karuwan and S. Muncharoen, Application of Chitosan@ Fe3O4 Nanoparticle-Modified Screen-Printed Graphene-Based Electrode for Simultaneous Analysis of Nitrite and Ascorbic Acid in Hydroponics and Fruit Juice, *Sensors*, 2025, **25**(5), 1431, DOI: 10.3390/s25051431.

33 B. Shobana, K. Renugadevi and P. Prakash, A high sensitive microbial photoelectrochemical sensor based on Cuprous oxide@ Titanium Dioxide/MXene for the selective detection of Staphylococcus aureus in polymicrobial environment, *J. Electroanal. Chem.*, 2025, **977**, 118857, DOI: 10.1016/j.jelechem.2024.118857.

34 I. Ghouafria, A. R. Nadji, B. Bezzina, H. Ferkous, N. Bengourna, H. Tahraoui, A. Amrane, A. Delimi, C. Boulechfar and A. Kahlouche, Sustainable corrosion protection: Unveiling Cystoseirasedoides as a high-performance green inhibitor for carbon steel: Experimental and computational studies, *Mater. Today Commun.*, 2025, **47**, 112900, DOI: 10.1016/J.MTCOMM.2025.112900.

35 I. Lakikza, H. Ghodbane, M. L. Chelaghmia, A. Boublia, S. I. Aouni, I. Belkhettab, H. Ferkous, A. Erto, A. S. Bentalib and Y. Benguerba, Unraveling the corrosion inhibition mechanisms of Algerian Dryopterisfilix mas leaf extract on A210C carbon steel in 1 M HCl: Comprehensive insights from electrochemical, morphological, XPS, and theoretical analyses, *Mater. Today Commun.*, 2025, **42**, 111262, DOI: 10.1016/J.MTCOMM.2024.111262.

36 S. Boukerche, H. Ferkous, A. Delimi, A. Sedik, A. Djedouani, K. OtmaneRachedi, H. Bouchoukh, M. Berredjem, M. Zahzouh, A. Himour, S. Bellucci, M. Alam and Y. Benguerba, Anti-corrosion performance of dehydroacetic acid thiosemicarbazone on XC38 carbon steel in an acidic medium, *Arab. J. Chem.*, 2023, **16**, 105061, DOI: 10.1016/J.ARABJC.2023.105061.

37 N. Mouats, S. Djellali, H. Ferkous, A. Sedik, A. Delimi, A. Boublia, K. O. Rachedi, M. Berredjem, A. Çukurovali, M. Alam, B. Ernsti and Y. Benguerba, Comprehensive Investigation of the Adsorption, Corrosion Inhibitory Properties, and Quantum Calculations for 2-(2,4,5-Trimethoxybenzylidene) Hydrazine Carbothioamide in Mitigating Corrosion of XC38 Carbon Steel under HCl Environment, *ACS Omega*, 2024, **9**, 27945–27962, DOI: 10.1021/acsomega.3c10240.

38 S. Boudjelida, D. Souad, F. Hana, Y. Benguerba, C. Imane and C. Mauro, Physicochemical Properties and Atomic-Scale Interactions in Polyaniline (Emeraldine Base)/Starch Bio-Based Composites: Experimental and Computational Investigations, *Polymers*, 2022, **14**, 1505–15051514, DOI: 10.3390/POLYM14081505.

39 M. Oubaaqa, M. Ouakki, M. Rbaa, A. Elgendy, R. Idouhli, M. Maatallah, A. Jarid, M. E. Touhami, B. Lakhrissi and A. Zarrouk, Two pyran derivatives as corrosion inhibitors for mild steel in HCl solution: Experimental and theoretical investigations, *Mater. Today Commun.*, 2023, **35**, 106188, DOI: 10.1016/J.MTCOMM.2023.106188.

40 T. Himeur, K. Rouibah, H. Ferkous, A. Boublia, K. O. Rachedi, K. Harrouche, C. Boulechfar, A. Abdennouri and Y. Benguerba, Unlocking the power of InulaViscosa essential oil: A green solution for corrosion inhibition in XC48 steel within acidic environments, *Process Saf. Environ. Prot.*, 2024, **187**, 1422–1445, DOI: 10.1016/J.PSEP.2024.05.061.

41 N. Ramdane, Z. Marsa, A. Delimi, A. Sedik, A. Boublia, G. S. Albakri, M. Abbas, K. K. Yadav, M. Gabsi, A. Djedouani, K. O. Rachedi, L. Toukal, H. Benzouid, M. Berredjem, H. Ferkous and Y. Benguerba, Synergistic shielding of copper from nitric acid corrosion: Unveiling the mechanisms through electrochemical, characterization, and computational insights with 2-Hydroxybenzaldehyde oxime, *Inorg. Chem. Commun.*, 2024, **165**, 112479, DOI: 10.1016/J.INOCHE.2024.112479.

42 D. Siziani, Y. Abdi, B. Bezzina, Z. Attou, N. Bensouilah and B. Boutemeur, A combined theoretical and experimental investigation on the solvatochromism of fused chromene-furanopyran: Determination of dipole moments, DFT/TD-DFT, chemical reactivity and Fukui Function, *J. Mol. Struct.*, 2025, **1319**, 139473, DOI: 10.1016/J.MOLSTRUC.2024.139473.

43 H. Ferkous, K. Rouibah, N. E. H. Hammoudi, M. Alam, C. Djilani, A. Delimi, O. Laraba, K. K. Yadav, H. J. Ahn, B. H. Jeon and Y. Benguerba, The Removal of a Textile Dye from an Aqueous Solution Using a Biocomposite Adsorbent, *Polymers*, 2022, **14**, 2396, DOI: 10.3390/POLYM14122396.

44 K. OtmaneRachedi, H. Ferkous, I. Ghouafria, B. Bezzina, A. Sedik, A. Delimi, A. Abdennouri, A. Djedouani, A. Houssou, H. Benzouid, A. Oral, Y. Benguerba, M. Berredjem, Unmasking the Latent Roles of Novel 3-(4-Carboxyphenyl) Iminoethyl-4-Hydroxy-6-Methyl-2-Pyrone Schiff Base as Corrosion Inhibitors for Xc38 Steel in Acidic Conditions: *Electrochemical and Computational Studies*, 2025, DOI: 10.2139/SSRN.5336995.

45 A. Madaci, H. Ferkous, A. Sedik, A. Delimi, C. Boulechfar, A. Belakhdar, M. Berredjem, M. A. Chaouch, M. Alam, H. Majdoub, N. Jaffrezic-Renault and Y. Benguerba, Experimental and theoretical study of polysaccharides extracted from prickly pear nopales Pulp (PPUN) of Opuntiaficus-indica as corrosion inhibitors, *J. Mol. Liq.*, 2023, **384**, 122272, DOI: 10.1016/J.MOLLIQ.2023.122272.

46 E. Kurtulbaş, Z. Ciğeroğlu, S. Şahin, N. El Messaoudi and V. Mehmeti, Monte Carlo, molecular dynamic, and experimental studies of the removal of malachite green using g-C3N4/ZnO/Chitosan nanocomposite in the presence of a deep eutectic solvent, *Int. J. Biol. Macromol.*, 2024, **274**, 133378, DOI: 10.1016/J.IJBIOMAC.2024.133378.

47 K. Rouibah, H. Ferkous, M. Abdessalam-Hassan, B. L. Mossab, A. Boublia, C. Pierlot, A. Abdennouri, I. Avramova, M. Alam, Y. Benguerba and A. Erto, Exploring the Efficiency of Algerian Kaolinite Clay in the Adsorption of Cr(III) from Aqueous Solutions: Experimental and Computational Insights, *Molecules*, 2024, **29**, 2135, DOI: 10.3390/MOLECULES29092135.

48 M. R. Makhlouf, M. Bendjaballah, I. Boukerche, I. Kouadri, S. Hamidoud, M. E. H. Benhamza and H. Hammi, Eco-friendly synthesis of biosorbent based in chitosan-activated carbon/zinc oxide nanoparticle beads for efficiency reduction of cadmium ions in wastewater, *Biomass Convers. Biorefinery*, 2025, **15**(8), 12001–12016, DOI: 10.1007/s13399-024-05960-0.

49 B. Shobana and P. Prakash, Sensitive rutin detection at nanomolar levels utilizing CeO2/BaO@ Ti3C2Tx nanocomposite-based photoelectrochemical sensor, *Mater. Sci. Semicond. Process.*, 2025, **186**, 109035, DOI: 10.1016/j.mssp.2024.109035.

50 R. Jenkins, and R. L. Snyder, *Introduction to X-ray powder diffractometry*, New York, Wiley, 1996, 138,403, DOI: 10.1002/9781118520994.

51 H. Ferkous, M. Zerroug, M. A. Chaouch, M. Radjai, H. Majdoub and A. Bouzid, Green Corrosion Inhibitor for Carbon Steel in 1 M HCl: A Comparative Study of Polysaccharides Extracted from Prickly Pear Nopals of OpuntiaFicus-Indica (Peel and Pulp), *Adv. Sci. Technol. Innov.*, 2018, 1293–1296, DOI: 10.1007/978-3-319-70548-4_380.

52 K. Laouameur, A. Flilissa, C. eddineLemaoui, H. Ferkous and Y. Benguerba, Study of the effect of current intensity on the structural performance of electrogeneratedmesoporous aluminum phosphate: application for adsorption, *Environ. Sci. Pollut. Res.*, 2023, **30**, 27510–27524, DOI: 10.1007/S11356-022-23578-5/METRICS.

53 A. Houssou, S. Amirat, H. Ferkous, S. Alleg, K. Dadda, R. Boulechfar, L. Abadlia, W. Bouchelaghem, J. K. Bhutto, M. A. Alreshidi, K. K. Yadav, N. Elboughdiri, A. Erto and Y. Benguerba, Experimental and computational investigations on mechanically alloyed Fe55Co30Ni15 powders, *Powder Technol.*, 2024, **433**, 119203, DOI: 10.1016/J.POWTEC.2023.119203.

54 A. Belakhdar, S. Djellali, H. Ferkous, B. Bezzina, A. Boublia, M. Berredjem, Y. Ben Amor, B. Ernst, M. Alam and Y. Benguerba, Comprehensive study of synergistic corrosion inhibition for XC48 steel in acidic medium using cistuscreticus extract and iodide ions: Integrative experimental and computational analysis, *J. Taiwan Inst. Chem. Eng.*, 2026, **178**, 106383, DOI: 10.1016/J.JTICE.2025.106383.

55 H. Behloul, H. Ferkous, N. Bougdah, S. Djellali, M. Alam, C. Djilani, A. Sedik, D. Lerari, B. H. Jeon and Y. Benguerba, New insights on the adsorption of CI-Reactive Red 141 dye using activated carbon prepared from the ZnCl2-treated waste cotton fibers: Statistical physics, DFT, COSMO-RS, and AIM studies, *J. Mol. Liq.*, 2022, 364, DOI: 10.1016/j.molliq.2022.119956.

56 F. Bouchareb, M. Berredjem, D. A. Dehmchi, R. Kadri, M. Kadri, H. Ferkous, A. Mansouri, S. Bouyegh, S. A. Ahmed, T. Ben Hadda and R. Bahadi, Synthesis, characterization, DFT/M06 studies, NBO, QTAIM and RDG analyses of new copper (II) complexes with bis-phosphonamide obtained under microwave irradiation, *J. Mol. Struct.*, 2023, **1294**, 136503, DOI: 10.1016/J.MOLSTRUC.2023.136503.

57 Z. Sun, L. Liu, D. Jia zeng and W. Pan, Simple synthesis of $CuFe_2O_4$ nanoparticles as gas-sensing materials, *Sensor. Actuator. B Chem.*, 2007, **125**, 144–148, DOI: 10.1016/j.snb.2007.01.050.

58 K. Atacan, M. Özacar and M. Özacar, Investigation of antibacterial properties of novel papain immobilized on tannic acid modified Ag/$CuFe_2O_4$ magnetic nanoparticles, *Int. J. Biol. Macromol.*, 2018, **109**, 720–731, DOI: 10.1016/j.ijbiomac.2017.12.066.

59 B. S. Surendra, Green engineered synthesis of Ag-doped CuFe2O4: Characterization, cyclic voltammetry and photocatalytic studies, *J. Sci. Adv. Mater. Devices*, 2018, **3**, 44–50, DOI: 10.1016/j.jsamd.2018.01.005.

60 B. Shobana, K. Renugadevi and P. Prakash, Label-free Photoelectrochemical detection of Aspergillus flavus in food samples using $NiFe_2O_4$@ $Ti_3C_2T_x$ nanocomposite with an ultra-low detection limit, *Microchem. J.*, 2025, 114684, DOI: 10.1016/j.microc.2025.114684.

61 F. Bouchareb, M. Berredjem, D. A. Dehmchi, R. Kadri, M. Kadri, H. Ferkous, A. Mansouri, S. Bouyegh, S. A. Ahmed, T. Ben Hadda and R. Bahadi, Synthesis, characterization, DFT/M06 studies, NBO, QTAIM and RDG analyses of new copper (II) complexes with bis-phosphonamide obtained under microwave irradiation, *J. Mol. Struct.*, 2023, **1294**, 136503, DOI: 10.1016/J.MOLSTRUC.2023.136503.

62 H. Ferkous, A. Delimi, A. Kahlouche, C. Boulechfar, S. Djellali, A. Belakhdar, K. K. Yadav, I. H. Ali, A. Ahmad, H. J. Ahn, M. H. Abdellattif, B. H. Jeon and Y. Benguerba, Electrochemical and Computational Approaches of Polymer Coating on Carbon Steel X52 in Different Soil Extracts, *Polymers*, 2022, **14**, 3288, DOI: 10.3390/POLYM14163288/S1.

63 B. Wang, S. Gu, Y. Ding, Y. Chu, Z. Zhang, X. Ba, Q. Zhang and X. Li, A novel route to prepare LaNiO 3 perovskite-type oxide nanofibers by electrospinning for glucose and hydrogen peroxide sensing, *Analyst*, 2012, **138**, 362–367, DOI: 10.1039/C2AN35989H.

64 H. Boucheta, E. Zouaoui, H. Ferkous, A. Madaci, K. K. Yadav and Y. Benguerba, Advancing Diabetes Management: The Future of Enzyme-Less Nanoparticle-Based Glucose Sensors-A Review, *J. Diabetes Sci. Technol.*, 2025, **19**(4), 1097–1108, DOI: 10.1177/19322968241236211.

65 Z. H. Sheng, X. Q. Zheng, J. Y. Xu, W. J. Bao, F. Bin Wang and X. H. Xia, Electrochemical sensor based on nitrogen doped graphene: Simultaneous determination of ascorbic acid, dopamine and uric acid, *Biosens. Bioelectron.*, 2012, **34**, 125–131, DOI: 10.1016/J.BIOS.2012.01.030.

66 S. Qi, B. Zhao, H. Tang and X. Jiang, Determination of ascorbic acid, dopamine, and uric acid by a novel electrochemical sensor based on pristine graphene, *Electrochim. Acta*, 2015, **161**, 395–402, DOI: 10.1016/J.ELECTACTA.2015.02.116.

67 K. Z. Brainina, M. A. Bukharinova, N. Y. Stozhko, S. V. Sokolkov, A. V. Tarasov and M. B. Vidrevich, Electrochemical Sensor Based on a Carbon Veil Modified by PhytosynthesizedGold Nanoparticles for Determination of Ascorbic Acid, *Sensors*, 2020, **20**, 1800, DOI: 10.3390/S20061800.

68 S. Babu, R. Kathirvel and P. Periakaruppan, Photoelectrochemical Detection of Penicillium spp. using

MgFe2O4@ V2CTx for Ensuring Food Safety, *Food Biosci.*, 2025, **71**, 107392, DOI: 10.1016/j.fbio.2025.107392.

69 L. Bourouba, E. Zouaoui, M. Benounis, H. S. Magar and A. Boumaza, A highly accurate and selective non-enzymatic glucose sensor based on a Fe_2O_3/$CuFe_2O_4$/graphene nanoplatelet nanocomposite, *RSC Adv.*, 2025, **15**(49), 41546–41567, DOI: 10.1039/D5RA07666H.

70 P. C. Motsaathebe and O. E. Fayemi, Electrochemical Detection of Ascorbic Acid in Oranges at MWCNT-AONP Nanocomposite Fabricated Electrode, *Nanomaterials*, 2022, **12**, 645, DOI: 10.3390/NANO12040645.

71 B. Gu, Z. Liu, X. Wang and X. Dong, RF magnetron sputtering synthesis of carbon fibers/ZnO coaxial nanocable microelectrode for electrochemical sensing of ascorbic acid, *Mater. Lett.*, 2016, **181**, 265–267, DOI: 10.1016/J.MATLET.2016.06.055.

72 C. Dehchar, I. Chikouche, R. Kherrat, S. Zougar and A. Zouaoui, Electrocatalytic Oxidation Of Ascorbic Acid At Polypyrrole Thin Film Incorporating Palladium Particles, *Surf. Rev. Lett.*, 2017, **24**, DOI: 10.1142/S0218625X17501189.

73 B. Shobana, K. Renugadevi and P. Prakash, Transformative microbe (E. Coli O157: H7) detection: Advancing microbial surveillance in food matrices with a photosensor of silver doped titanium dioxide/MXene nanocomposite, *Microchem. J.*, 2024, **206**, 111461, DOI: 10.1016/j.microc.2024.111461.

74 Y. Ding, C. Ren, X. Tian, M. Zhang, J. Zhang, K. Sun, Y. Wu, H. Sun, L. Pang and F. Sha, Facile synthesis of aminophenylboronic decorated electrospun CoFe2O4 spinel nanofibers with enhanced electrocatalytic performance for glucose electrochemical sensor application, *Ceram. Int.*, 2021, **47**, 19052–19062, DOI: 10.1016/J.CERAMINT.2021.03.251.

75 N. Pal, B. Saha, S. K. Kundu, A. Bhaumik and S. Banerjee, A highly efficient non-enzymatic glucose biosensor based on a nanostructured NiTiO3/NiO material, *New J. Chem.*, 2015, **39**, 8035–8043, DOI: 10.1039/C5NJ01341K.

76 A. G. Solangi, A. Tahira, A. S. Chang, T. Pirzada, Z. A. Solangi, F. Chang and Z. H. Ibupoto, Enhanced electro active properties of NiCo2O4 nanostructures using garlic extract for the sensitive and selective enzyme-free detection of ascorbic acid, *J. Mater. Sci.: Mater. Electron.*, 2023, **34–20**, 1549, DOI: 10.1007/s10854-023-10937-2.

77 H. S. Magar, A. M. Fahim and M. S. Hashem, Accurate, affordable, and easy electrochemical detection of ascorbic acid in fresh fruit juices and pharmaceutical samples using an electroactive gelatin sulfonamide, *RSC Adv.*, 2024, **14**, 39820–39832, DOI: 10.1039/D4RA06271J.

78 H. Guan, S. Du, B. Han, Q. Zhang and D. Wang, A rapid and sensitive smartphone colorimetric sensor for detection of ascorbic acid in food using the nanozyme paper-based microfluidic chip, *LWT-Food Sci. Technol.*, 2023, **184**, 115043, DOI: 10.1016/J.LWT.2023.115043.

79 A. Belakhdar, R. Ayeche, H. Behloul, H. Ferkous, A. Boublia, A. Hallati, S. Boufassa, A. Abdennouri, K. O. Rachedi, A. Kahlouche and Y. Benguerba, Green corrosion inhibition of XC48 steel in acidic media using prickly pear oil extract: electrochemical, thermodynamic, and computational insights, *J. Mol. Struct.*, 2026, **1349**, 143860, DOI: 10.1016/J.MOLSTRUC.2025.143860.

80 H. Ferkous, S. Guezane-Lakoud, A. Sedik, A. Boublia, A. Delimi, A. Kahlouche, C. Boulechfar, Y. Dilgin, K. S. A. Halim, M. Albrahim and Y. Benguerba, Tailored α-hydroxyphosphonate derivatives: Green synthesis, spectroscopic characterization, DFT analysis, and high-efficiency corrosion protection for copper in acidic media, *Sustain. Mater. Technol.*, 2025, **43**, e01282, DOI: 10.1016/J.SUSMAT.2025.E01282.

81 K. Rouibah, H. Ferkous, F. Z. Akika, A. Boublia, D. Bousba, A. Gouasmia, I. Belal, K. S. Abdel Halim, M. Albrahim and Y. Benguerba, Adsorption and solar photocatalytic degradation of naphthalene by α-Fe2O3/ZnFe2O4 nanoparticles: Experimental and DFT insights, *J. Phys. Chem. Solids*, 2025, **207**, 112848, DOI: 10.1016/J.JPCS.2025.112848.

82 N. Benachour, A. Delimi, H. Allal, A. Boublia, A. Sedik, H. Ferkous, A. Djedouani, S. Brioua, C. Boulechfar, H. Benzouid, A. Houssou, A. Oral, B. Ernst, M. Alam and Y. Benguerba, 3,4-Dimethoxy phenyl thiosemicarbazone as an effective corrosion inhibitor of copper under acidic solution: comprehensive experimental, characterization and theoretical investigations, *RSC Adv.*, 2024, **14**, 12533–12555, DOI: 10.1039/D3RA08629A.

83 A. Rizi, A. Sedik, A. Acidi, K. O. Rachedi, H. Ferkous, M. Berredjem, A. Delimi, A. Abdennouri, M. Alam, B. Ernst and Y. Benguerba, Sustainable and Green Corrosion Inhibition of Mild Steel: Insights from Electrochemical and Computational Approaches, *ACS Omega*, 2023, **8**, 47224–47238, DOI: 10.1021/ACSOMEGA.3C06548.

84 C. Boulechfar, A. Toghan, H. Ferkous, A. Djedouani, A. Delimi, A. Kahlouche and D. S. El Sayed, Multifaceted insights into novel three-aromatic Schiff Base as a potential corrosion inhibitor for copper and Brass in 1M HCl solution, *Inorg. Chem. Commun.*, 2025, 116030, DOI: 10.1016/j.inoche.2025.116030.

85 S. Brioua, A. Delimi, H. Ferkous, S. Boukerche, H. Allal, A. Boublia, A. Djedouani, M. Berredjem, A. Kahlouche, K. O. Rachedi, A. Abdennouri, M. Alam, B. Ernst and Y. Benguerba, Enhancing corrosion resistance of XC38 steel using sulfur and nitrogen-containing phenyl thiosemicarbazone: A comprehensive experimental and computational analysis, *J. Taiwan Inst. Chem. Eng.*, 2024, **165**, 105718, DOI: 10.1016/j.jtice.2024.105718.